Intensity Interferometry with Fresnel Lens Telescopes — Design, Construction and First Observations with MI²SO

Master's Thesis in Physics

by
Christopher Ingenhütt
03.12.2024

Erlangen Center for Astroparticle Physics
Friedrich-Alexander-Universität Erlangen-Nürnberg

Supervisor: Prof. Dr. Stefan Funk

Abstract

In this thesis, the viability of Fresnel lens telescopes for use in intensity interferometry is examined and tested with observations. The Mobile Intensity Interferometer for Stellar Observations is designed based on constraints given by point spread function measurements of the 1 m diameter and $f/1.2$ Fresnel lenses and the intention to construct a low-complexity lightweight instrument.

Observation parameters such as the expected photon rate and signal-to-noise are simulated for bright stars visible from the Northern hemisphere in summer. The stars showing the highest expected achieved significance in simulations — Arcturus and Vega — are chosen as observation targets.

Observations of Arcturus and Vega are carried out at a center wavelength of 655 nm in clear nights. Measurement data from the observation nights is correlated offline. The photon bunching peaks are analyzed using three different approaches modeling the time resolution of the system.

Photon bunching peaks are detected in observations for both stars, demonstrating the viability of small aperture Fresnel lens telescopes. Using the dataset of 8 h and 40 min obtained in observations across four nights in July, the angular diameter of Arcturus is determined to 20.84 ± 0.63 mas, lying within 5.5 % of the literature value for 700 nm.

Contents

1 Theory

Intensity Interferometry (II) is a method of high angular resolution astronomy developed in the 1950s by Robert Hanbury Brown and Richard Twiss [1]. Initially, II was doubted as a method of high angular resolution astronomy due to the nature of underlying effects (see section 1.6) being unexpected behavior with the understanding of light at the time. However, Hanbury Brown and Twiss demonstrated its practicability and succeeded in establishing the method, using it to measure the angular diameters of several stars at optical wavelengths [2]. In the following section, the mechanisms at play and theoretical background necessary for this method are explained.

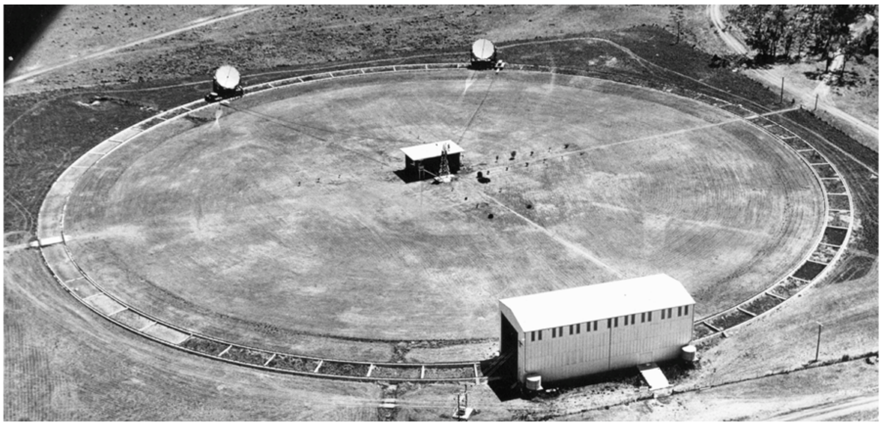

Figure 1: The Narrabri Stellar Intensity Interferometer. Two telescopes are mounted on a circular railway track to vary their distance to each other.

1.1 Historical background and motivation

II is a measurement technique related to and derived from the same principal characteristics of (partially) coherent light as amplitude interferometry. In the following section, the advantages of both amplitude- and intensity interferometry relative to direct imaging methods and each other will be demonstrated. A point source viewed by any optical system, be it lenses or mirrors, produces an Airy pattern in the image plane, setting a limit on the angular resolution with which a star's extent can be measured. This Airy pattern occurs due to the light from distant point sources arriving as plane waves onto the "slit", a telescope's aperture [3].

Figure 2 shows the Fraunhofer diffraction of plane waves of light. The pattern resulting from a circular "slit" in three dimensions is called an Airy pattern of bright central Airy disc and concentric circles of alternating minima and side maxima in intensity. The resolution limit is governed by the wavelength λ of light observed and the aperture D of the instrument.

The Rayleigh criterion (equation 1[4]) determines the smallest angular separation $\Delta\theta$ between two objects at which they are resolvable as separate objects. The criterion determines this to be the case when the maximum (or center) of one object's Airy pattern falls into the first minimum of the second object's Airy pattern.

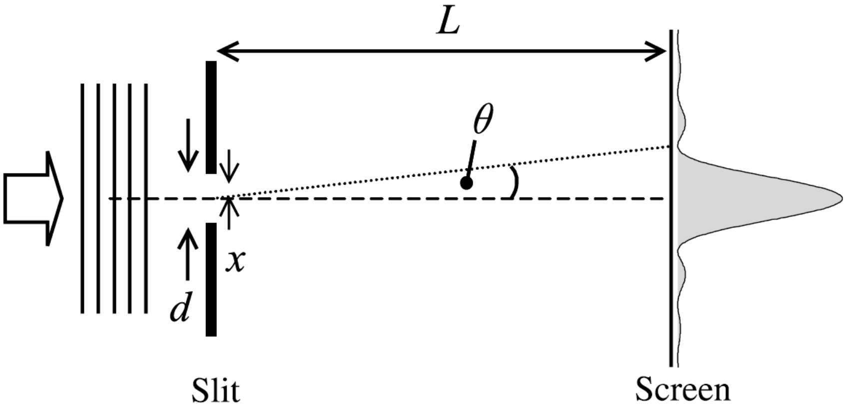

Figure 2: Fraunhofer diffraction of plane wave light impacting a slit.

$$\Delta\theta = 1.22\lambda/D \tag{1}$$

As is obvious from the above equation, larger aperture diameters D are necessary to resolve smaller objects. However, telescopes cannot be built with arbitrarily large diameters due to the prohibitive cost and technical challenge of constructing precise (and precisely controlled moving) and structurally sound lenses or mirrors of diameters necessary to resolve anything smaller than close supergiant and giant stars. Even supergiants at a distance of $\sim 1\,\mathrm{kpc}$ already require aperture diameters close to a hundred meters, making a direct imaging approach unfeasible.

This problem motivated the development of the field of amplitude interferometry. Instead of a "single slit" aperture directly imaging the target object, the Michelson interferometer acts as a double slit producing an interference pattern. The position of the minimum in this pattern is now no longer dependent on the size of the light-collecting mirrors, but rather the distance between them. Expanding this to extended sources and not point sources, there will be overlapping interference patterns on the image plane of the interferometer. If the distance between the mirrors d is larger than the necessary distance from the Rayleigh criterion (equation 1) $d > 1.22\lambda/\delta\theta$, the light collected by the two primary mirrors interfering in the image plane will be spatially incoherent and no clear fringes of an interference pattern will be visible. By varying the distance d and observing fringe visibility, the angular diameter of the star can thus be probed[5].

By using this technique, the problem of larger apertures being necessary to resolve smaller stars was circumvented. However, the interference pattern produced in the image plane is still subject to distortions caused before impacting the mirror — specifically atmospheric turbulence produces a limiting factor to the absolute resolution of this technique and presents challenges to compensate in real time. Furthermore, the distance d between the mirrors needs to be known with precision to the order of the observed wavelength. Current generation amplitude interferometers achieve resolutions of $\Delta\theta = 0.2\,\mathrm{mas}$ at red wavelengths $\lambda = 640\,\mathrm{nm}$ [6]. The unit mas refers to milliarcseconds, or $\frac{1}{1000}\,'' = \frac{1}{3600000}\,^{\circ}$.

Figure 3 illustrates the light path taken in the Michelson interferometer at Mount Wilson, taken from [7]. It was the first interferometer of its kind utilized for amplitude interferometry. The distance between mirrors M_1 and M_2 is called baseline, and can be

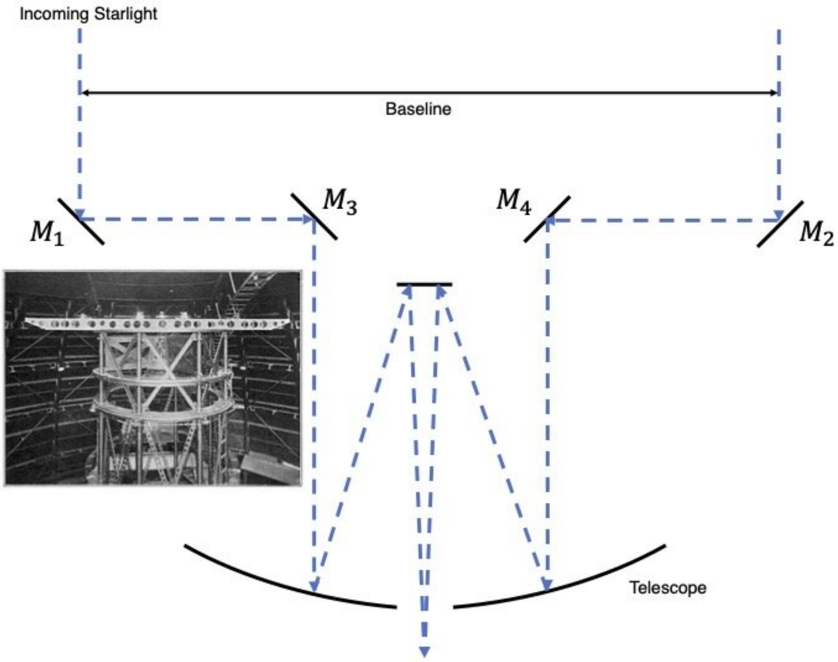

Figure 3: Schematic of the Michelson interferometer. Light collected at mirrors M_1 and M_2 is reflected and aligned to interfere in the image plane.

varied to examine the interference behavior and the maximum in visibility of interference fringes determines the resolution of this design.

Intensity Interferometry eliminates both the effects of atmospheric turbulence on the light's phase impacting the resolution as well as the necessity for submicrometer precision in telescope positions by measuring light *intensity* rather than *amplitude*. In essence, the telescopes merely collect light and count the rate at which photons are collected, ignoring the phase of the star's light arriving at Earth (see section 1.7.1). However, due to the nature of chaotic light sources such as stars, pure intensity information recorded at different positions still holds information about the geometry of the source. The following sections will explain how to extract this information.

1.2 The geometry of multiple telescope observations

In figure 3 the distance between mirrors is referred to as baseline. This is equivalent to the physical distance between the telescopes for light originating from a star lying perpendicular to the connecting line between the two telescopes — for example at zenith, or 90 ° altitude for two telescopes on even ground. However, as soon as the telescopes of an interferometer, be it an amplitude or intensity interferometer, are not pointing at a star in a direction perpendicular to their combined viewing plane, one needs to instead consider the *projected* baseline and optical path delay.

Figure 4 illustrates the projected baseline from the direction of the star as well as the path delay present. In an amplitude interferometer, both of these have to be corrected for in real time to take into account their effects on interference fringe visibility. In an intensity interferometer, they still play an important role, but can be calculated after

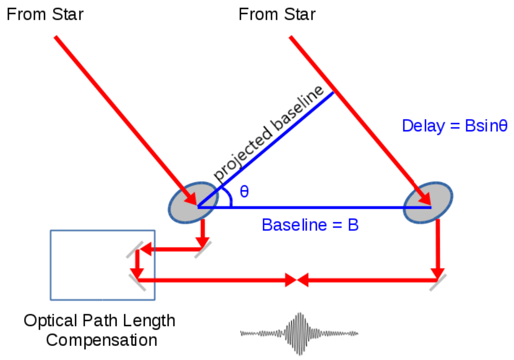

Figure 4: Projected baseline and optical path delay illustrated for off-zenith observations. Figure adapted from [8].

the measurement run, offline, provided knowledge of the relative telescope positions and the target's path in the sky. In II, one can get rid of the concept of optical path delay by defining coincidence as times separated by precisely the optical path delay experienced at observation time.

1.3 Coherence

Incoherent light still interferes, however the interference patterns resulting are random. Therefore, all interferometric measurement techniques can only work on coherent light. Coherence is not a binary quality of light, but rather a scale of how well knowledge about the light's amplitude and phase at one measurement in time and space informs predictions of amplitude and phase at a different time and space. Measures for the time and distance over which a prediction becomes inaccurate are called coherence time τ_c and coherence length $l_\mathrm{c} = c\tau_\mathrm{c}$. The correlation of amplitude and phase at different times is called temporal coherence, at different positions spatial coherence.
The coherence time τ_c describes the time period within which the phase of a wave packet remains stable or predictable from knowledge of it at a point in time within said period. Electromagnetic waves change their phase periodically by their wavelength, therefore a wave packet consisting of waves of one wavelength (monochromatic) would have infinite coherence time, as knowledge of the phase at any point in time could predict the phase at every other point in time. The coherence time can be defined as the inverse of the optical bandwidth (in frequency, not wavelength) [9].

$$\tau_\mathrm{c} = \frac{1}{\Delta\omega} \tag{2}$$

This can still be expressed in terms of bandwidth in the wavelength domain, however, frequency bandwidth as a function of wavelength bandwidth contains the center wavelength. Therefore, coherence time as a function of optical bandwidth in the wavelength domain also contains the center wavelength.

$$\tau_\mathrm{c} = \frac{1}{\Delta\omega} = \frac{1}{\frac{d\omega}{d\lambda}|_{\lambda_0} \cdot \Delta\lambda} = \frac{\lambda_0^2}{c\Delta\lambda} \tag{3}$$

Coherence time becomes shorter with broader optical bandwidth, therefore it is prudent to filter incoming starlight.

1.4 First- and second-order correlation functions

The first- and second-order correlation functions are used to describe coherence in a quantified manner. The first-order correlation function $g^{(1)}(\tau)$ describes a quantified degree of temporal and spatial coherence based on the properties of the first power of the electric field [10]:

$$g^{(1)}(r_1, r_2, \tau) = \frac{\langle \mathcal{E}^*(r_1, t)\mathcal{E}(r_2, t+\tau)\rangle}{\sqrt{\langle |\mathcal{E}(r_1, t)|^2\rangle \langle |\mathcal{E}(r_2, t)|^2\rangle}} \tag{4}$$

With $\langle \cdots \rangle$ denoting time average, $\mathcal{E}(r_{\mathrm{i}}, t)$ electric field at positions r_i and τ time difference. The field is averaged over a large (relative to τ) amount of time. This function describes the spatial and temporal coherence at different points at time differences τ. Since the distance between detectors is orders of magnitude smaller than the distance to the source, intensities at the two detector positions can be assumed equal and the denominator can be simplified to the time-averaged intensity at one position r_1 (by convention):

$$g^{(1)}(r_1, r_2, \tau) = \frac{\langle \mathcal{E}^*(r_1, t)\mathcal{E}(r_2, t+\tau)\rangle}{\langle I_1(t)\rangle} \tag{5}$$

The second-order correlation function $g^{(2)}(r_1, r_2, \tau)$ quantifies coherence based on light intensities or the second power of electric fields [11]:

$$g^{(2)}(r_1, r_2, \tau) = \frac{\langle \mathcal{E}^*(r_1, t)\mathcal{E}^*(r_2, t+\tau)\mathcal{E}(r_2, t+\tau)\mathcal{E}(r_1, t)\rangle}{\langle \mathcal{E}^*(r_1 t)\mathcal{E}(r_1, t)\rangle\langle \mathcal{E}^*(r_2, t+\tau)\mathcal{E}(r_2, t+\tau)\rangle} = \frac{\langle I(r_1, t)I(r_2, t+\tau)\rangle}{\langle I(r_1, t)\rangle\langle I(r_2, t+\tau)\rangle} \tag{6}$$

If one interprets the light intensity's time dependence as fluctuations around an average intensity $I(t) = \langle I(t)\rangle + \Delta I(t)$ and uses $\langle a+b\rangle = \langle a\rangle + \langle b\rangle$ as well as $\langle const \cdot a\rangle = const \cdot \langle a\rangle$ this simplifies to:

$$g^{(2)}(r_1, r_2, \tau) = \frac{\langle \langle I_1\rangle\langle I_2\rangle + \langle I_1\rangle \Delta I_2 + \langle I_2\rangle \Delta I_1 + \Delta I_1 \Delta I_2\rangle}{(\langle I_1\rangle + \langle \Delta I_1\rangle)(\langle I_2\rangle + \langle \Delta I_2\rangle)} = \frac{\langle\langle I_1\rangle\langle I_2\rangle\rangle + \langle \Delta I_1 \Delta I_2\rangle}{\langle I_1\rangle\langle I_2\rangle} \tag{7}$$

Several terms become zero because they contain time averages over the intensity fluctuation $\langle \Delta I(t)\rangle = 0$, allowing further simplifying to:

$$g^{(2)}(r_1, r_2, \tau) = \frac{\langle\langle I_1\rangle\langle I_2\rangle\rangle}{\langle I_1\rangle\langle I_2\rangle} + \frac{\langle \Delta I_1 \Delta I_2\rangle}{\langle I_1\rangle\langle I_2\rangle} = 1 + \frac{\langle \Delta I_1 \Delta I_2\rangle}{\langle I_1\rangle\langle I_2\rangle} \tag{8}$$

1.5 Data analysis — from light intensities to $g^{(2)}(r_1, r_2, 0)$

Photodetectors, specifically Photo Multiplier Tubes (PMTs) aim to detect (with varying detection efficiency) the amount of incident photons over a counting or integration time. The response of these devices in count rate $R(t)$ or PMT current is directly proportional to the intensity of incident light [12], allowing a definition of an un-normalized $g^{(2)}$

function dependent only on measurable quantities:

$$g^{(2)}(r_1, r_2, \tau) = \frac{\langle R_1(t) R_2(t+\tau) \rangle}{\langle R_1(t) \rangle \langle R_2(t+\tau) \rangle} \tag{9}$$

If these detectors are then synced ($\tau = 0$), the function becomes the spatial second-order correlation function for light collected in two PMTs at some distance:

$$g^{(2)}(r_1, r_2, 0) = \frac{\langle R_1 R_2 \rangle}{\langle R_1 \rangle \langle R_2 \rangle} \tag{10}$$

1.6 Photon bunching and the HBT effect

With the second-order correlation function laid out as a measurable quantity, the question remains how light from an extended thermal (chaotic) source such as a star behaves in these correlation functions. From equation 8, three different cases are observed:

- $\frac{\langle \Delta I_1 \Delta I_2 \rangle}{\langle I_1 \rangle \langle I_2 \rangle} = 0$, the fluctuations in the intensities at different positions average out, distribution of light is random. This character of light is called **coherent**.
- $\frac{\langle \Delta I_1 \Delta I_2 \rangle}{\langle I_1 \rangle \langle I_2 \rangle} < 1$, fluctuations in the intensities at different positions are negatively correlated, it is less likely to detect a photon in detector 2 coincident with a photon in detector 1. This character of light is called **antibunched**.
- $\frac{\langle \Delta I_1 \Delta I_2 \rangle}{\langle I_1 \rangle \langle I_2 \rangle} > 1$, fluctuations in the intensities at different positions are positively correlated, it is more likely to detect "bunches" of photons than single ones. This character of light is called **bunched**.

1.6.1 Coherent light

Coherent light such as from a monochromatic source is characterized by $g^{(2)}(r_1, r_2, \tau) = 1$ for all values of τ. Detections at all possible time differences between the detectors and positions within the light beam are equally probable. Monochromatic lasers exhibit this character [13].

1.6.2 Antibunched light

Antibunched light does not contain bunches of photons in the stream that are closer together. Rather, there is a suppression effect present on photon pairs closer in time than the coherence time τ_c. Time differences between arrival times are to an extent random, however do not fall below a minimum value. This type of light can be observed if an individual emitter is isolated (an atom, molecule etc) and the emission rate controlled via fluorescence. Due to individual emitters being subject to a lifetime characteristic to the photon-emitting transition, the time interval between emissions has a clear floor that cannot be bypassed, resulting in a time period of antibunched light [14].

1.6.3 Bunched light

Bunched light brings us to the Hanbury Brown and Twiss (HBT) effect. Let us consider first the limited case of purely temporal correlation $r_1 = r_2$:

$$g^{(2)}(\tau) = \frac{\langle I(t)I(t+\tau)\rangle}{\langle I(t)\rangle^2} \tag{11}$$

For large values of τ under the assumption of a stable light source this simplifies to:

$$g^{(2)}(\tau \gg \tau_\mathrm{c}) = \frac{\langle I(t)\rangle^2}{\langle I(t)\rangle^2} = 1 \tag{12}$$

And for simultaneous detections $\tau = 0$:

$$g^{(2)}(0) = \frac{\langle I(t)^2\rangle}{\langle I(t)\rangle^2} \tag{13}$$

No matter the precise shape of the intensity's time dependence, this term needs to be $g^{(2)}(0) \geq 1$ and $g^{(2)}(0) \geq g^{(2)}(\tau)$. Therefore, the temporal second-order correlation function of such a light source is a strictly monotonically decreasing one, falling from some finite value to 1 over the timescale of the coherence time τ_c.

Furthermore, the specific cases of Doppler- and collision-broadened chaotic light exhibit a Gaussian (Doppler) and Lorentzian (collision) shape above 1, with both reaching $g^{(2)}(0) = 2$, see figure 5. The effect of collision-broadening refers to frequency spectra broadening emission lines due to collisions of neighbouring emitters (atoms or molecules), while Doppler-broadening refers to spectra broadened by each emitter's relative velocity to the observer. While both Doppler- and collision-broadening is present in starlight, the

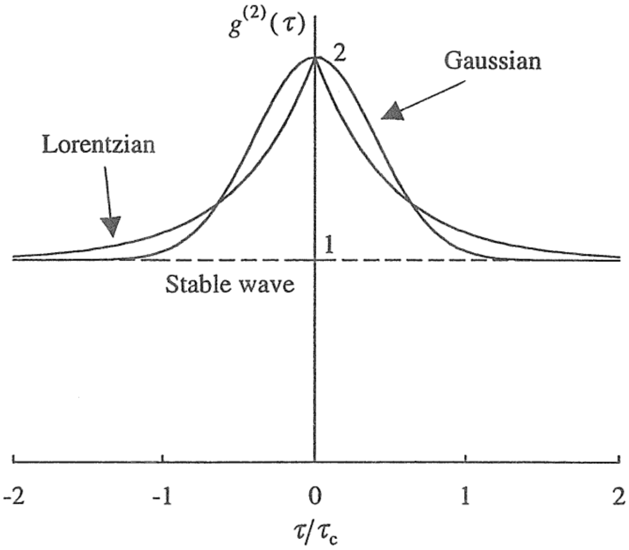

Figure 5: $g^{(2)}(\tau)$ of Doppler-, collision-broadened and coherent light sources. Doppler-broadened light sources follow a Gaussian, collision-broadened a Lorentzian distribution. The dashed line indicates the constant $g^{(2)}(\tau)$ of a coherent light source. Figure from [15].

high kinetic energy of the individual emitters inside a star makes Doppler-broadening the clearly dominant effect. Perfectly coherent, monochromatic light is subject to no spectrum broadening effects and does not exhibit a peak in $g^{(2)}(\tau)$.

1.7 Important relations and theorems

1.7.1 Siegert relation

For chaotic light from Gaussian processes of a macroscopic number of atoms, the first- and second-order correlation functions can be directly linked (technically any order of correlation function can be) using the Siegert relation.

$$g^{(2)}(r_1, r_2, \tau) = 1 + |g^{(1)}(r_1, r_2, \tau)|^2 \tag{14}$$

This in turn means a measured $g^{(2)}$ can inform knowledge about the first-order correlation function [16].

1.7.2 Van Cittert-Zernike theorem

This brings us closer to measuring angular diameters by using raw light intensities because the van Cittert-Zernike theorem in turn allows us to link the first-order correlation function with the geometry of the source [17].

When observing a planar light source in the far field, the spatial first-order correlation function is expressible in terms of the Fourier transform of the intensity distribution at the source:

$$g^{(1)}(r_1, r_2, 0) = \mathrm{e}^{ik(r_2 - r_1)} \frac{\int_\sigma I(r')\mathrm{e}^{-ik(s_2 - s_1)\cdot r'} d^2r'}{\int_\sigma I(r') d^2r'} \tag{15}$$

Using r_1 and r_2 as the locations of two detectors, k wave vector, source geometry σ and s_1, s_2 as two points in the source plane. Figure 6 illustrates the far field situation for which the equation 15 can be used to connect source geometry and $g^{(1)}(r_1, r_2, 0)$.

By inverting the Fourier transform, $g^{(1)}$ can be used to determine the geometry of the source for planar disc assumptions. The measurement of $g^{(2)}$ as done in II, using the Siegert relation and van Cittert-Zernike theorem, can be used to infer the source

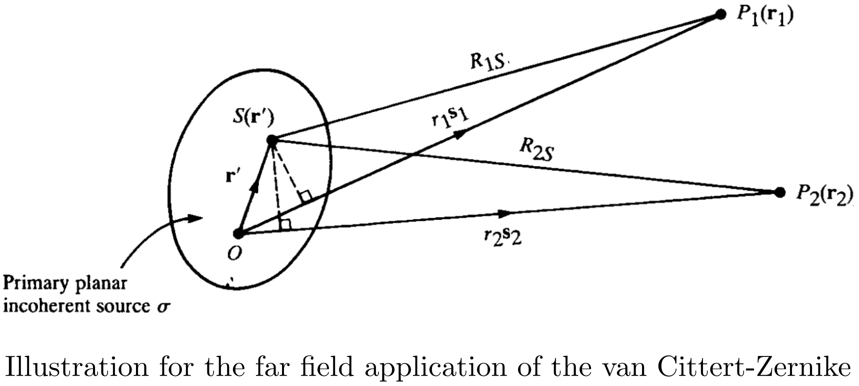

Figure 6: Illustration for the far field application of the van Cittert-Zernike theorem. $S(r')$ and O denoting points in the source plane, $P_1(r_1)$ and $P_2(r_2)$ detectors at different positions. Figure from [18]

geometry. However, since the Siegert relation only connects $g^{(2)}$ with $|g^{(1)}|^2$, phase information gets lost. Therefore, measurement of $g^{(2)}$ does not allow for a perfect transformation back to the source geometry σ.

If one is familiar with various functions describing diffraction, another useful parallel becomes clear: The first-order correlation function in the far field of an extended, chaotic/incoherent light source mirrors the Fraunhofer diffraction pattern for a coherent light source. Thus, for a circular aperture, one can determine the first- and second-order correlation functions to

$$g^{(1)}(r_1, r_2, 0) = \frac{2J_1(X)}{X} \tag{16}$$

and

$$g^{(2)}(r_1, r_2, 0) = 1 + \left|\frac{2J_1(X)}{X}\right|^2 \tag{17}$$

Where $X = \frac{\pi r_\star (r_2 - r_1)}{d_\star \lambda}$, $r_\star$ radius of the source and $d_\star$ distance between source and detector. J_1 is the first-order Bessel function. When the angular diameter θ is mentioned later, its small-angle approximation $\theta = \arcsin\frac{r_\star}{d_\star} \approx \frac{r_\star}{d\star}$ is used. All stellar sizes, including the sun, are sufficiently small for the relative error of this approximation to be irrelevant.

1.7.3 Wiener-Khintchine theorem

Finally, the Wiener-Khintchine theorem establishes a connection between the spectrum of the light source and the temporal first-order correlation function. Assuming $r_1 = r_2$ to get the purely temporal coherence, the source's power spectrum and $g^{(1)}(\tau)$ form a Fourier transform pair [19]:

$$g^{(1)}(\tau) = \int_{-\infty}^{\infty} F(\omega) \mathrm{e}^{-i\omega\tau} d\omega \tag{18}$$

Because the spectra of potential targets are either known or at the very least possible to model to good accuracy, using these spectra and the optical filters' transmission spectra allows the calculation of key characteristics in the signal. Specifically the timescale on which $g^{(2)}$ falls from 2 to 1 can be calculated by applying the Fourier transform to a filtered source spectrum.

In the example case of a rectangular frequency spectrum — meaning the spectral bandwidth is small enough that the star's output can be assumed constant across the bandwidth and a perfect band filter with 0% transmission outside of it's band — this timescale τ_1 is equal to the first zero of the sinc function.

$$g^{(2)}(\tau) = 1 + \mathrm{sinc}^2\left(\frac{\tau \Delta\omega}{2}\right) \tag{19}$$

Since optical filters are typically characterized in the wavelength domain, the timescale becomes $\tau_1 = \frac{\lambda_0^2}{\Delta\lambda \cdot c}$. From this it is apparent that this method has much lower requirements in time resolution for long wavelengths and optical filters with narrow bandwidths.

1.8 Angular resolution and signal strength of Intensity Interferometers

As has been demonstrated so far, the $g^{(2)}$ function for light coming from a distant source can be measured (equation 10) and translated into the squared absolute of the

$g^{(1)}$ function (equation 14). The measured peak in the $g^{(2)}$ function of two separate, but time-synced detectors ($r_1 \neq r_2$ and $\tau = 0$) in units of time is defined as:

$$\tau_{\text{meas}} := \int_{-\infty}^{\infty} (g^{(2)}(r_1, r_2, 0) - 1) d\tau = \left| g^{(1)}(r_1, r_2, 0) \right|^2 \tag{20}$$

From this measure, one can finally make conclusions about the geometry of the light source (equation 15). Going into practical situations with generalized transmission spectra, II can measure the observed spatial coherence factor k_s at different detector distances (projected baseline b) and compare it to the theoretical expectation, fitting a spatial coherence curve with the form $\left|\frac{2J_1(X)}{(X)}\right|^2$ (see equation 17) [20].

$$\tau_{\text{meas}}(b) = k_{\text{pol}} k_\tau k_\text{s}(b) \frac{\lambda_0^2}{\Delta\lambda \cdot c} \tag{21}$$

Correction factor $k_{\text{pol}} = 0.5$ stems from the unpolarized nature of the light beam and is constant. Correction factor k_τ corresponds to differences in expected coherence time due to deviations from a perfectly rectangular filter transmission spectrum and is constant for observations of the same underlying spectrum with the same filter. For sufficiently narrow bandwidth $\Delta\lambda$ of the filter, it can additionally be assumed constant across different targets. Correction factor $k_\text{s}(b)$ is defined as the degree of spatial coherence at a projected baseline b, normalized to $k_\text{s}(0) = 1$ and $k_\text{s}(b \geq 1.22\frac{2r_\star\lambda}{d_\star}) = 0$, falling with the shape of the squared first-order Bessel function. While J_1 (and k_s)b)) does indeed have side maxima, the squaring of the function results in these being generally too low to detect outside of extremely high statistics measurements for particularly bright stars. Furthermore, these side maxima would lie at even higher projected baselines than the first minimum. The measured quantity τ_{meas} does not describe the coherence time changing with baseline, but rather is a measurement for the spatial coherence in the same unit as coherence time.

When it comes to the question of angular resolution of an intensity interferometer it makes intuitive sense to define it similarly to the Rayleigh criterion (equation 1) of the first minimum of k_s and therefore $\tau_\text{c}(b)$. As with amplitude interferometry, the telescope apertures are of no consequence to this and the baseline b determines the limit of angular resolution. Because the measured data in II is merely photon count rates — the correlation can be performed offline — the limit for angular resolution is determined by the limit in distance for which two detectors can be time synchronized to sufficient precision (at least same order of magnitude as time resolution). This is a significantly less constricting demand for precision than the corresponding one in amplitude interferometry, pertaining to the precision knowledge of the baseline between telescopes. Figure 7 illustrates once more the difference in setup for amplitude- and intensity interferometry.

Using fiber connected White Rabbit nodes, sub-nanosecond precision should be achievable for kilometer baselines, resulting in angular resolutions down to $\Delta\theta \approx 25\,\mu\text{as}$.

The size of the collecting apertures is however very relevant for the signal-to-noise ratio (S/N) achieved [22].

$$S/N \propto A \alpha_{\text{qe}} \alpha_{\text{trans}} R_\star k_\text{A} k_\text{s} k_{\text{pol}} F(\omega) \sqrt{\frac{T\Delta\omega}{2\sigma_\text{t}}} \tag{22}$$

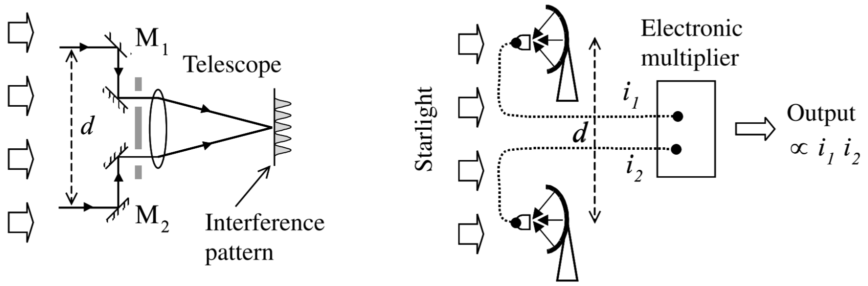

Figure 7: Functional schematic of an amplitude interferometer (left) and an intensity interferometer (right). An amplitude interferometer brings light collected at the two mirror positions M_1 and M_2 into interference while an intensity interferometer correlates the intensities collected at the two telescope positions. Figure from [21].

With A collection area, α_{qe} quantum efficiency, α_{trans} filter transmission, $R_\star$ photon rate of the star per unit time, area and optical bandwidth, k_{A} a correction factor relating to spatial coherence losses based on aperture size, T observation time and σ_{t} time resolution [23].
For all practical values of filter widths at optical wavelengths, the timescale of the $g^{(2)}$ peak τ_1 from equation 19 is to the order of picoseconds:

$$\tau_1 = \frac{(560\,\text{nm})^2}{1\,\text{nm} \cdot c} = 1.05\,\text{ps} \tag{23}$$

However, the time resolution of PMTs is typically in the hundreds of picoseconds. Due to this, the photon bunching peak observed will never reach $g^{(2)} = 2$, but be much smaller in amplitude and quiet electronics are of high importance. Intuitively, filters of minimal bandwidth seem optimal for these measurements, however due to the dependence on the photon rate, losses due to wide filters in τ_1 affecting the size of the peak are counterbalanced by gains from the sheer amount of photons.
Finally, one can recall equation 17 as the intended measured quantity. After the corrections for various factors, the resulting peak integral in the $g^{(2)}$ function for some projected baseline $b = r_2 - r_1$ can be fitted to a function

$$k_{\text{s}}(b) = \left| \frac{2 \cdot A \cdot J_1(\frac{\pi\theta b}{\lambda_0})}{\frac{\pi\theta b}{\lambda_0}} \right|^2 \tag{24}$$

with the amplitude A in unit coherence time and θ stellar angular diameter. The amplitude A can also be predicted based on instrumentation since the coherence time is an instrument-specific value independent of the target. This quantity is called the zero-baseline coherence.

1.9 Fresnel lenses

Fresnel lenses refer to lenses manufactured to contain the curvature of a classical lens segment-wise on one face of the lens. This design reduces the amount of material drastically at the cost of optical quality. There are aberrations expected to arise from the borders between curved segments, however, optical quality is of secondary concern for II due to the requirements merely being a light collecting aperture focusing a target star's light onto a photodetector.

Figure 8 shows this structure schematically — on a real Fresnel lens the segments would be significantly smaller, resulting in drastically reduced lens thickness and therefore weight. As an example, just one mirror facet used in the Imaging Air Cherenkov Telescopes (IACTs) at the High Energy Stereoscopic System (H.E.S.S.) weighs 15 kg at 60 cm diameter [25], the 100 cm diameter $f/1.2$ Fresnel lens used in this project weighs only ~ 2.8 kg and stands at a thickness of just 3 mm. This very low thickness and weight is achieved partially through the Fresnel lens structure and partially through material choice — Fresnel lenses can be manufactured from acryllic, reducing the weight further from a glass Fresnel lens at the expense of transparency. Typically, the clear acrylic used results in lens transmission to the order of 90 %. The material choice and small volume of an acrylic Fresnel lens also ultimately lead to a shorter manufacturing and testing process as for example mirror facets require, and a much lower cost. For these reasons, the feasability of using Fresnel lenses in an intensity interferometer was tested in this project.

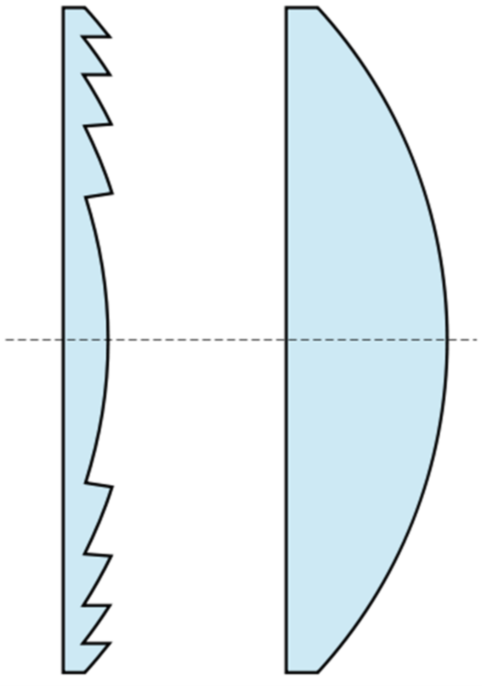

Figure 8: Schematic of Fresnel lens compared to classical lens, taken from [24]. The size of the curved segments is exaggerated for illustration purposes.

2 Design and Construction of MI²SO

With the theoretical background laid out, we can now look towards what the considerations mean for the design of an intensity interferometer. This section details the path of the *Mobile Intensity Interferometer for Stellar Observations* (MI²SO) from two 1 m diameter Fresnel lenses to operation on the roof of the Erlangen Center for Astroparticle Physics (ECAP) building.

After attempts to use 55 cm diameter Fresnel lens telescopes (the same as are in use in the IceAct telescopes) as an intensity interferometer at ECAP, two larger Fresnel lenses were acquired to increase photon rates and consequently signal-to-noise. Figure 9 shows the finished telescopes for MI²SO in operation, taking data at very low elevation.

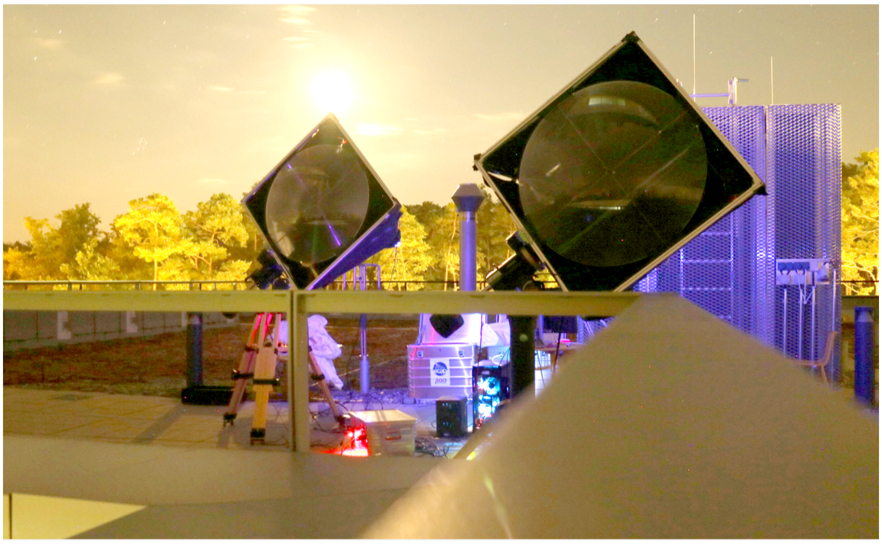

Figure 9: MI²SO in operation on the roof of ECAP observing Arcturus in a moonlit night.

2.1 Fresnel lens point spread function and photomultiplier choice

While it had previously been established that MI²SO would use photomultiplier tubes (PMTs) as detectors, the choice of model was an open question, depending on both geometric considerations as well as potentially target-dependent wavelength band considerations (see section 3.3). In a first step, the size of the lenses' focal spot (their point spread function, PSF) needed to be determined. Too wide of a PSF could lead to edge effects on the photocathode of the chosen PMT or worse — part of the target star's light being focused onto the PMT housing with no chance of detection. Out of three different PMT models in question for this project, two had detector surfaces of $(23 \times 23)\,\mathrm{mm}^2$ and one had a detector surface of $(14 \times 14)\,\mathrm{mm}^2$. The measurement of the PSF aimed to determine whether the latter detector surface was large enough to capture most of the focused light. To this end, the radius of the smallest circle containing 90 % of the light in the focal plane, r_{90} was measured.

For this measurement a 35 m long mirror test laboratory with two optical benches was used. This room is situated in the basement of the ECAP building with no windows, allowing operations in complete darkness. At one end of the laboratory, an LED was set up on the first optical bench aligned with the center of the lens on the other optical bench. The second optical bench at the other end of the room carried the lens, a plexiglass screen and a camera behind it to view the focal plane.

Initial attempts to determine the detector surface area needed to efficiently receive starlight focused by the lens were carried out by attempting to approximate a 1 m diameter beam of parallelized light of homogenous flat field intensity. To test the homogeneity of the intensity profile of the light, it was projected onto a screen and analyzed with the raw brightness data of the blue pixels of a Basler acA2500-60uc USB camera (for documentation see [26]). Images were cropped to represent the circular end of the lightcone captured and to be parallelized by the Fresnel lens. As a measure of how homogenous or "flat" the intensity profile was, the relation between standard deviation and mean brightness value $\frac{\sigma}{\mu}$ was calculated. This relation is called relative variability in the following.

The unmodified LED had a relative variability of $\sim 137\,\%$, with a vastly brighter central region as expected from the shape of the LED. The front of the LED acting as a lens was then filed off to a flat surface using fine sandpaper, see figure 10 for a comparison between unmodified and filed flat LED. Filing off the plano convex lens at the front of the LED resulted in a reduction in relative variability to $\sim 22.9\,\%$.

In the next step towards approximating a flat field, a pinhole and diffusor were added in front of the filed off LED. This again resulted in a reduction in relative variability to $\sim 17.5\,\%$. Finally, a greyscale of this intensity distribution (see figure 11) was printed

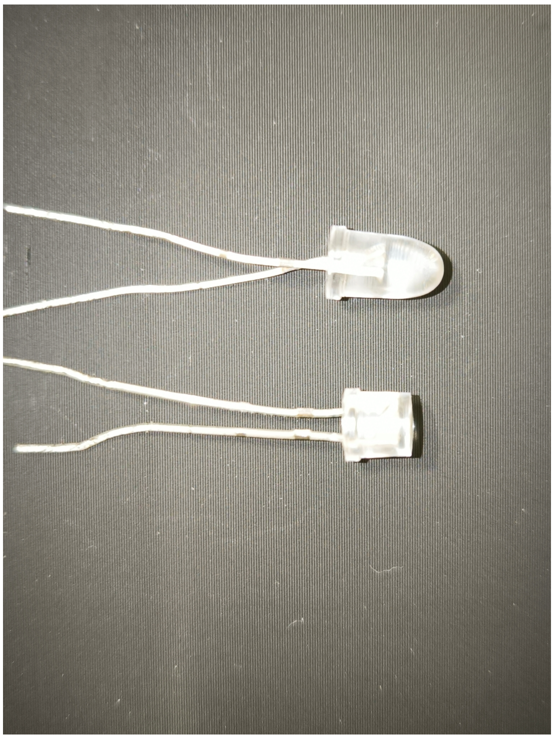

Figure 10: LEDs with lens front and filed flat.

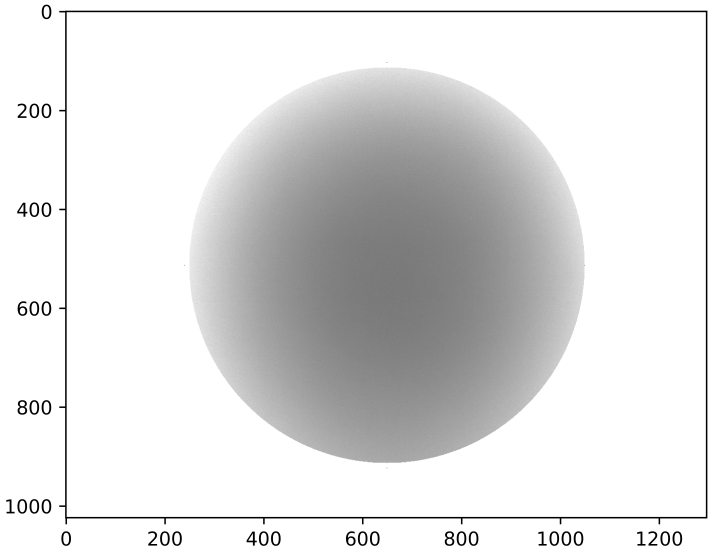

Figure 11: Brightness values of blue pixels in image of lightcone produced by filed off LED and diffusor. Greyscale was normalized to give the brightest pixel a value of 100 % black, with all other pixels directly scaled by their relative brightness to the maximum.

on transparent film and aligned with the LED at the distance where this distribution was of the same size as the film. Both the transparent film and the plexiglass screen can be seen in figure 12 inside their 3D-printed holding frames used to position them on the optical benches. The holding frames contain holes at the bottom to insert aluminium rods that can be screwed to the optical benches to facilitate placing of both the film and screen at the correct height. This greyscale film reduced the relative variability of intensity to less than 5 % when properly aligned with the lightcone.

One of the Fresnel lenses was then set up at its focal length from the LED, with the grooved side towards it to parallelize the light cone flattened in intensity distribution by the diffusor and film. This represents Fresnel lenses' more common use case: typically, they are used to parallelize light beams in lighthouses to provide a constrained light beam over long distances. Figure 13 shows the resulting situation at the second optical bench. The parallelized light beam is focused by the Fresnel lens (left side of the image) onto the plexiglass screen (center of the image) and the shadow at the wall behind the bench (right side of the image) shows a slightly wider light beam than the lens.

Ultimately, this setup was deemed to not accurately measure the PSF of one lens due to the imperfect flat field intensity as well as unknown parallelization capabilities of the Fresnel lens — it effectively measured the PSF of one lens and the parallelization of the other lens at the same time. Figure 14 shows a schematic view of the setup. Not to relative scale, blue lines illustrate the light cone and parallelized beam assuming perfect parallelization.

The setup was then adjusted to only use one lens and the LED was made to mimic a "point source" to the same order in size as stars that could potentially be observed. For this purpose, a 1 mm diameter pinhole was placed in front of the LED. At the distance

Figure 12: Transparent film with greyscale light intensity distribution printed on and plexiglass screen inside 3D-printed holding frames.

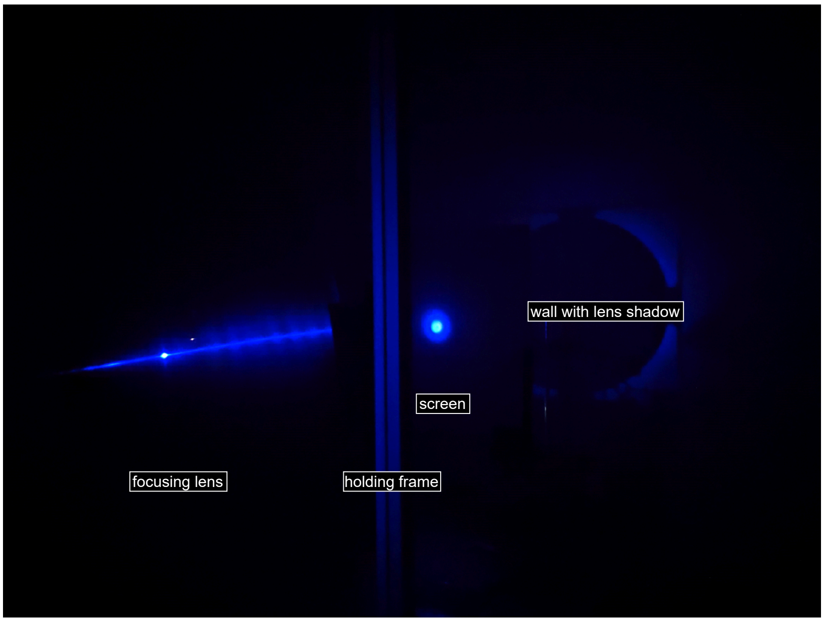

Figure 13: Intensity homogenized and parallelized light beam impacting Fresnel lens, imaging screen and shadow at the wall behind it.

of the optical benches, this resulted in an effective angular diameter of 0.1 as, which corresponds roughly to twice the size of Betelgeuse.

Figure 15 shows the final setup used to determine the size of the focal spot of the Fresnel lens. This setup was validated using a smaller Fresnel lens with known PSF from earlier measurements [27] before measurements with the 1 m diameter lenses. The r_{90}

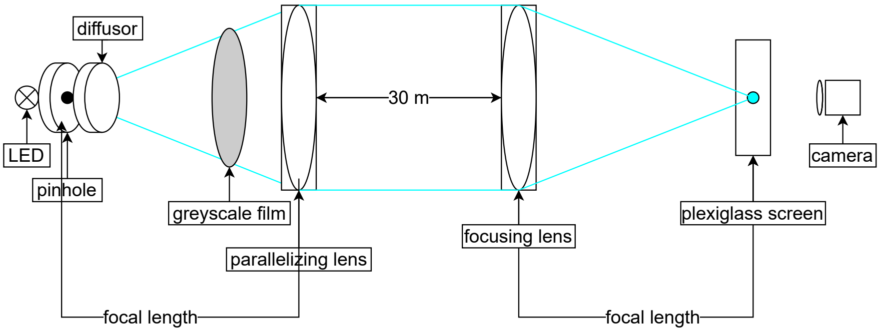

Figure 14: Test setup using approximated parallelized flat field from LED with highlighted components and distances.

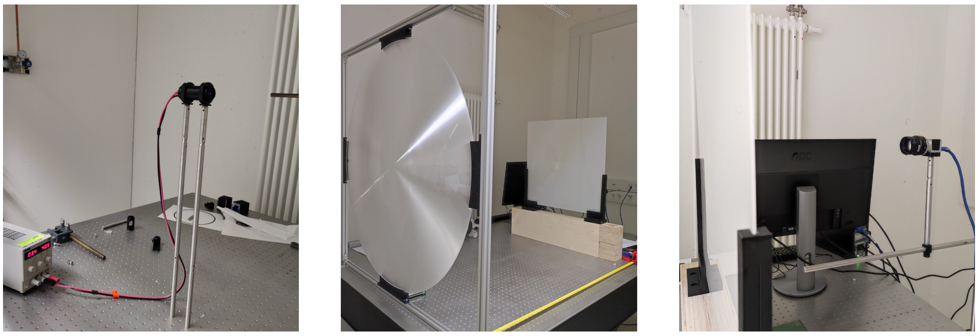

(a) LED on first optical bench.

(b) Fresnel lens and screen on optical bench 2.

(c) Camera viewing focal plane imaged on screen.

Figure 15: Lens point spread function measurement setup.

determined with the setup in the ECAP mirror test laboratory was within uncertainty the same as determined in Aachen.

After cropping the image to exclude reflections from the walls, floor and ceiling of the lab, a background image to be subtracted was created by taking 1000 images of the same exposure time with the lens covered and averaging the blue pixels' brightness values over these 1000 measurements. The average background image was then subtracted from 100 images with the lens uncovered to determine the radius containing 90 % of the light in the focal plane. With the standard deviation over 100 measurements as the uncertainty, the resulting PSF size was $r_{90} = 4.03 \pm 0.12\,\mathrm{mm}$.

Figure 16 shows the PSF of a randomly chosen measurement out of the hundred measurements done with r_{90} circle indicated in white. In further measurements, parts of the lens were covered to examine the homogeneity of the PSF. Both measurements with the outer 50 % of the lens covered and the inner 50 % resulted in unchanged (within uncertainty) r_{90} values.

With a focal spot smaller than 1 cm in diameter, not just the larger PMTs Hamamatsu R11265U-200 and R11265U-300 (datasheet see [28]) with detector surfaces of $(23 \times 23)\,\mathrm{mm}^2$ could be used, but the newer Hamamatsu H15461-40 (datasheet see [29]) with a smaller area of $(14 \times 14)\,\mathrm{mm}^2$ should still not contribute significant edge effects, provided the light is focused onto its center. Figure 17 shows the quantum efficiencies for R11265U-200 and R11265U-300 (subfigure 17a) and H15461-40 (subfigure

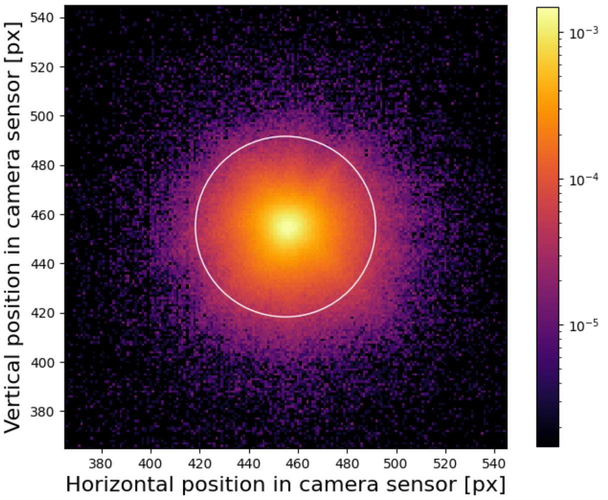

Figure 16: Fresnel lens PSF with r_{90}. Color gradient illustrates each pixel's contribution to total brightness.

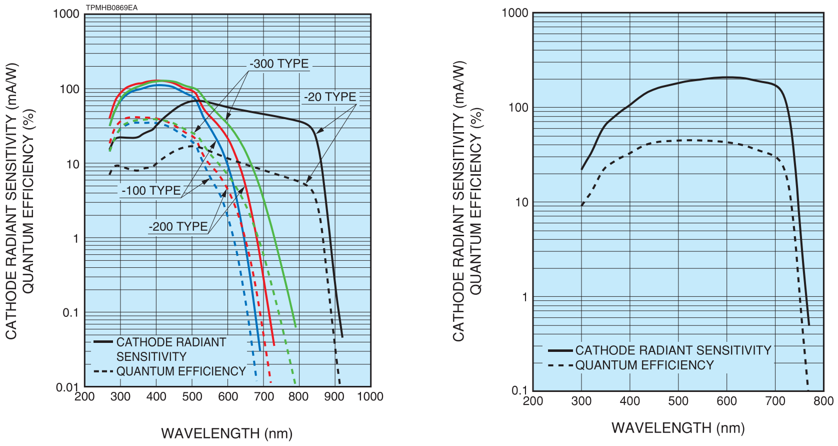

(a) Spectral response and quantum efficiency of Hamamatsu R11265U-series PMTs.

(b) Spectral response and quantum efficiency of Hamamatsu H15460-40 and H15461-40 PMTs.

Figure 17: Quantum efficiency for the candidate PMTs at wavelengths between 200 and 1000 nm. In the left plot, the red and green dashed lines indicate quantum efficiency for the R11265U-200 and R11265U-300 PMTs, respectively.

17b) PMTs. Due to the significantly better performance at longer wavelengths and comparable performance at shorter ones (quantum efficiency of $> 40\,\%$ at $\lambda = 600\,\mathrm{nm}$), the latter PMT model was chosen for use in MI²SO.

To further prevent edge effects and reduce night sky background, a pinhole the size of

$r_{\mathrm{ph}} = 4.5\,\mathrm{mm}$ was placed directly in front of the PMT. In this setup, it would therefore be expected to collect $\sim 95\,\%$ of the light into the PMT, provided the PMT housing being perfectly centered behind the lens.

2.2 Lens holding frame and general telescope structure

Already for the PSF measurements in section 2.1, the Fresnel lenses needed to be positioned in a stable holding frame on optical benches. Said holding frame was also to serve as the main structure of the MI^{2}SO telescopes. With two telescope mounts rated for stable tracking suited for astrophotography carrying up to 50 kg telescopes on them, weight was considered a potential problem as the large lens diameter (relative to its weight) as well as the focal length of 1.2 m created a much longer lever for the force of the telescope's weight. The two mounts used are Skywatcher EQ8-R and Skywatcher EQ8 (manuals see [30] and [31]). Both of the mounts are rated to 50 kg payloads and come with a counterweight axis and two 10 kg counterweights each. As the telescope dimensions exceed the length of the aforementioned counterweight axis, creating a longer lever, weight needed to be minimized where possible.

To achieve a low weight while not compromising too much on flexing instability, the lens holding frame was constructed from four $1060 \times 25 \times 25\,\mathrm{mm}$ aluminium profiles. Lens holders were 3D-printed from PLA plastic and fixated in the aluminium profiles using screws. Four lens holders were assembled from two 3D-printed parts, pressing on the lens cushioned by foam rubber. Figure 18 shows schematics for the holders. These holders are held together by screws and have sockets to insert carbon fiber rods arranged in a stabilizing cross behind (below it during operation of the telescope) the lens to reduce gravity-induced flexing of the lens itself.

Figure 19 shows the design of the telescope including lens holders, holding frame, carbon fiber rods, PMT housing, secondary stabilizing frame and mounting rail (in green).

To hold the detector in the focal spot, four carbon fiber rods were fixated to the lens holding frame's corners with 3D-printed sockets and a two-component adhesive. To

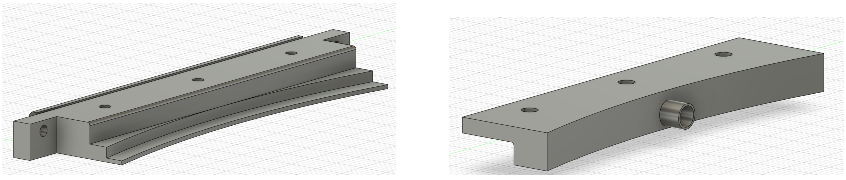

(a) Upper part of the lens holder to be positioned in front of the lens. Foam rubber was added to the strip in direct contact with the lens face. One of the screw holes used to fix these holders to the aluminium frame with t-nuts can be seen as well as three holes for screws to hold the two parts of the lens holder together.

(b) Lower part of the lens holder to be positioned behind the lens. Three holes for screws to hold the two parts of the lens holder together can be seen as well as the socket for one of the carbon fiber rods of the stabilizing cross.

Figure 18: Schematics of upper and lower part of the lens holders.

reduce flexing of the lenses, a cross of two carbon fiber rods was mounted behind the lens on the lens holders with a 3D-printed PLA plastic socket holding the lens center at level to its edges. Furthermore, to reduce flexing of the carbon fiber rod structure extending to the focal spot, a secondary stabilizing frame was constructed from five more carbon fiber rods glued into 3D-printed PLA plastic holders on the primary carbon fiber rods. This secondary stabilizing frame was then fixed to the mounting rail of the telescope mount using another 3D-printed PLA plastic part.

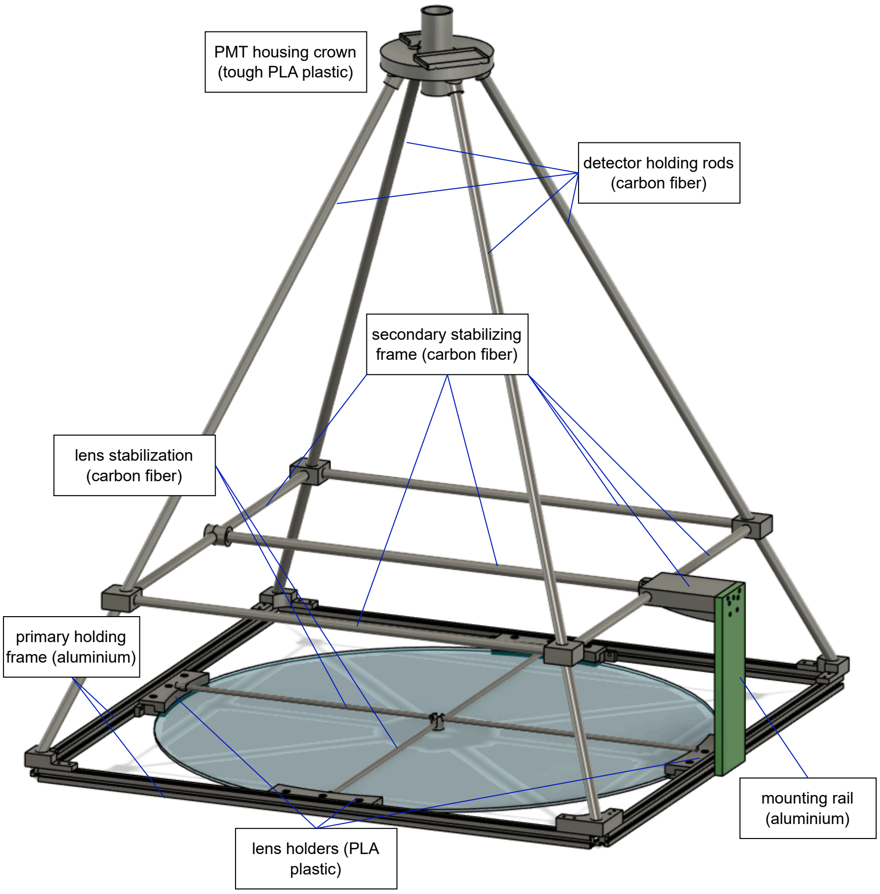

Figure 19: Schematic of the telescope design with highlighted parts.

2.3 PMT housing

Figure 20 shows the PMT housing crown design sans PMT and aluminium rails (which would extend below the crown in this figure). Two of the sockets used to glue it onto the carbon fiber rods are visible at the bottom.

Fresnel lenses are subject to strong chromatic aberration due to a strong wavelength dependence of the focal length. As the operating range of MI²SO is aiming to span the entire visual spectrum using different optical filters and possibly PMTs suited to each specific target, the distance of the detector surface from the lens needs to be adjustable. Therefore, a static PMT holder is not suited and instead a PMT "housing crown" was designed and 3D-printed with the adjustable distance as a key part in the design. This housing crown to be held in place by the carbon fiber rods was 3D-printed from a different material than other 3D-printed parts, tough PLA plastic. Stray sources of light off the primary target direction would end up focused in the focal plane around the PMT. In case of any accidental partial uncovering of the lenses during the day or strong light sources to the side being focused and producing significant heating power, a material with higher heat resistivity was chosen for any parts inside or close to the focal plane.

This PMT housing crown was glued to the carbon fiber rods using a two-component adhesive and contained four $d = 6\,\mathrm{mm}$ aluminium rods as rails for Thorlabs 2 inch tubing frames to be fixed in the middle. Using Thorlabs 2 inch and 1 inch tubes, the PMT, pinhole and optical filter were mounted inside the crown with their distance to the lens adjustable along the aluminium rods.

The Thorlabs 2 inch tubes were extended in front of the PMT to 5.6 cm. The opening angle of the optical system created by this tube extension was the same as the cone angle of focused light behind the lens. This way, the tubing system itself containing the optical filter, pinhole and PMT can assist in blocking stray light.

On the back of the PMT housing crown, two 3D-printed PLA plastic holders to carry the PMT's amplifier and gain control box were fixated using the screws holding the aluminium rails.

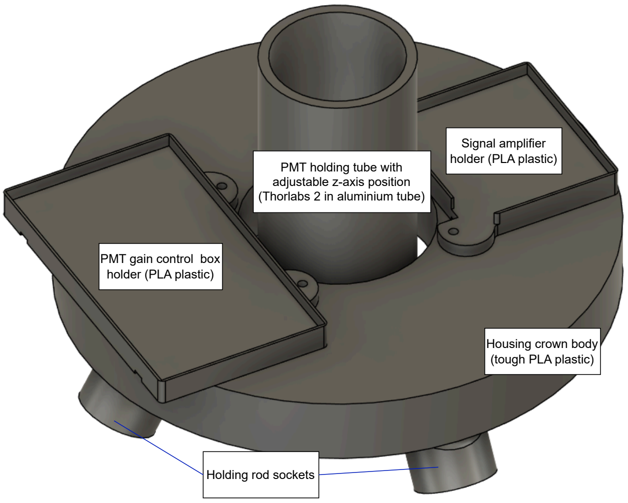

Figure 20: Schematic of the PMT housing crown with highlighted parts.

2.4 Cloth tubing and fogging prevention

Test operations of the telescopes revealed the necessity of further additions to the telescope design. Due to the instrument's position on top of the ECAP roof, a significant amount of stray light was present during the night, including the nearby biology department's greenhouse lighting, parking lot lights as well as an art installation. To reduce the amount of stray light captured by the telescopes, tubing was added from cloth previously used as darkroom curtains with 99 % internal reflectivity. This tubing

ended up a very effective choice while adding a very low amount of weight. The count rate of background light in the detectors was reduced by a factor of 5–8 by the addition of this tubing.
In humid nights, the lenses fogged up significantly, resulting in an increase in background count rate of almost tenfold from diffusely reflected stairwell lighting from inside the ECAP building. To prevent this effect, 4 m heating cables were installed at the secondary stabilizing frames. The cloth tubing added a stabilizing factor by reducing air circulation (and therefore cooling) inside the telescope. Figure 21 shows the telescopes operating in the final design observing Vega at high elevation. The lenses fogging up occured more often when observing at high altitudes. Whether this is an altitude dependent effect or simply due to higher humidity was not tested, but the heating cables behind the lens strongly mitigated the effect. Increased humidity correlated with observations at high altitudes due to the nights being typically more humid in the later hours. At this point in the night, Arcturus had already set below a treeline to the West of the ECAP roof. Vega stood at very high altitudes at those times and the fogging up of the lenses was only noticed during Vega observations. Also noticeable in the figure are the previously unmentioned guiding cameras mounted into the corner of the telescopes' lens frames (top right corner in of the front telescope, top left corner of the back telescope in the figure). The cameras used were one Starlight Xpress Lodestar Pro (for datasheet see [32]) and one Starlight Xpress Lodestar X2 (legacy handbook hosted at [33]). After roughly pointing at the target, guiding was temporarily disabled and the pointing direction manually adjusted at very low slewing speeds while monitoring the count rates in the detectors. When the count rates were at the maximum and stable with regards to small movements in either direction, guiding was re-enabled to keep the target focused.

Figure 21: MI^{2}SO in operation on the roof of ECAP observing Vega at high altitude. The black cloth tubing to block stray light such as from the moon (above one of the telescopes in the image) or artificial sources can be seen.

2.5 Measurement electronics

As mentioned in section 2.1, the detector chosen for MI²SO is the Hamamatsu H15461-40. From its datasheet (see [29]), the detection efficiency when operated at wavelengths around 655 nm lies around 40 %. For its time resolution, the transit-time spread (TTS) measured by Paul Blaß in [34] was used, on details for how this time resolution was taken into account, see section 4.1.3. This PMT was operated in current output mode, meaning the signal consisted of the PMT-amplified photon current. This signal was fed into a modified TA1000B-200 amplifier from the manufacturer FAST (datasheet of the unmodified version [35]). This modified amplifier provided an amplification factor of ~ 8.45 from testing data taken of the PMT operating alone and with the amplifier. Figure 22 illustrates the photon pulse data taken of the PMT (subfigure 22a) and the PMT amplified by the modified TA1000B-200 (subfigure 22b). For both of these setups, ~ 10000 pulses were recorded with the PMT covered. This setup shows the dark current and a very low rate of single photon pulses. By setting the trigger threshold, dark current was excluded and the peak area of single photon pulses (value of the peak in the histogram of this data) used calculate the gain in charge [36]. The histograms on the right of each subfigure clearly show only one peak, contrary to the expected two peaks if zero-photon events were not excluded by the trigger threshold.

This amplified signal was filtered by an analog lowpass filter, the model used being a Mini Circuits ZXLF-K221+ (datasheet see [37]). This model is a reflectionless low-pass filter with a cutoff frequency of 220 MHz. It was specifically chosen to reduce high frequency noise (the signal is expected to be detectable up to $\sim$ 200 MHz). Non-reflectionless filters introduce a lot of distortion on the pulse shape of the signal as well as ringing effects and possibly even secondary peaks. While the effects of this are deterministic, it was decided to use a reflectionless filter until a clear understanding of the effects (especially with different cable lengths changing the ringing frequency) could be gained to properly compensate for them in data analysis. Figure 23 shows the transmission of various filters, the used model in green [36].

As can be seen in the figure, the advantage of reflectionless filters comes at a cost to filtering capabilities and sharpness of the cutoff frequency. A transmission of -20 dB is only reached at frequencies of ~ 625 MHz, which is half the maximum sampling rate of the digitizer card. Because the filtering effect of these low-pass filters is rather modest, a digital low-pass filter was later introduced in the data analysis (see section 4.3).

The signal was then fed via different length Airborne 5 (datasheet see [38]) cables.

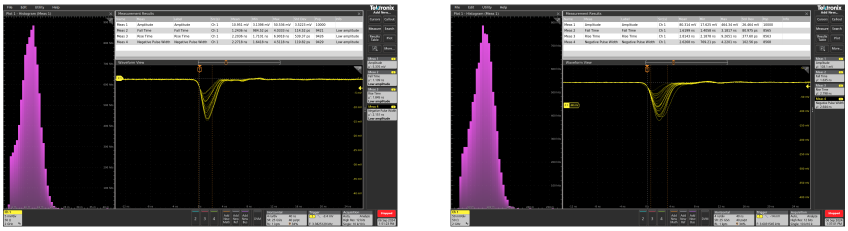

(a) Oscilloscope view of data taking process on unamplified PMT.

(b) Oscilloscope view of data taking process on PMT amplified by modified TA1000B-200.

Figure 22: Data taking process for modified amplifier gain measurement.

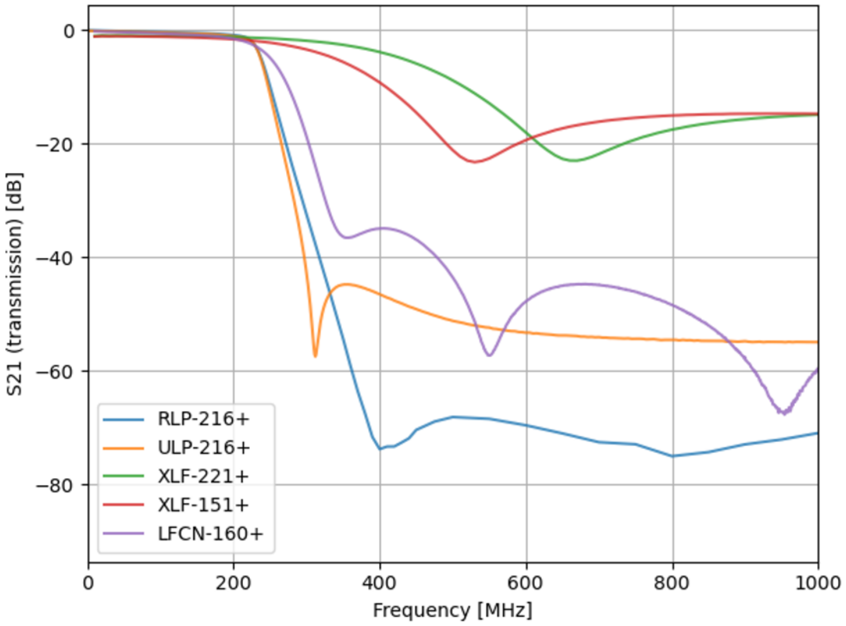

Figure 23: Transmission of various analog low-pass filter models at different wavelengths. Green and Red curve show reflectionless filters.

Cable lengths of 5 m and 40 m were chosen to offset the position of the photon bunching peak from the center. This was necessary because the signals from both telescopes were digitized by different channels on the same digitizer card (Spectrum M4i 2211-x8, [39]). This leads to significant crosstalk, multiple orders of magnitude stronger than the physical correlation signal.

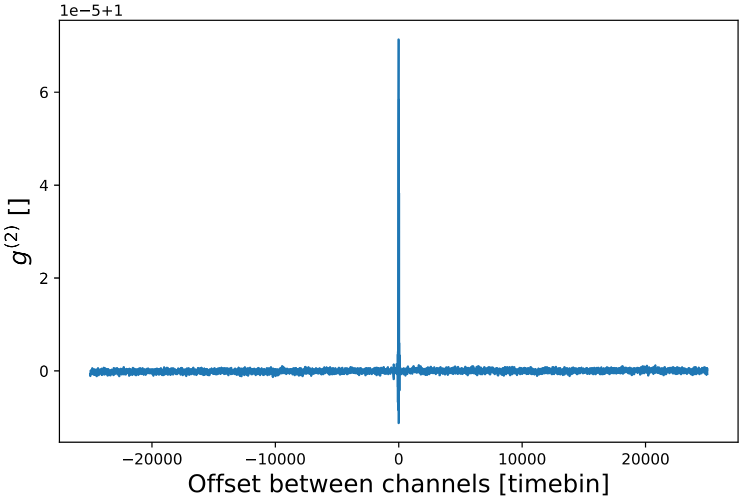

Figure 24: Example $g^{(2)}$ of a dataset illustrating the crosstalk due to the same digitizer receiving both signals.

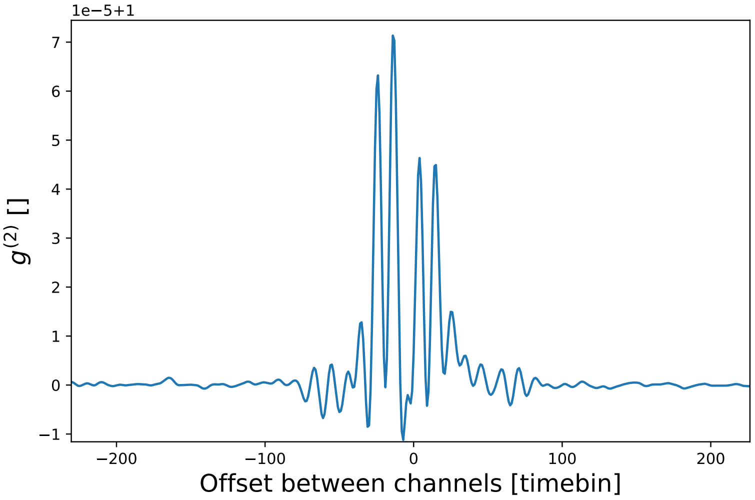

Figure 25: Zoomed in section of the example $g^{(2)}$. Photon bunching signal expected at offset of -172 timebins. y-axis scaled to crosstalk amplitude for illustration purposes.

Figure 24 shows an example $g^{(2)}$ for a dataset with the crosstalk region clearly visible in the center. This crosstalk region extends only some tens of nanoseconds to either side of the center of the $g^{(2)}$ function, making a known cable length difference an effective workaround. At the signal speed inside Airborne 5 cables, the photon bunching peak is expected $\sim 137\,\mathrm{ns}$ or ~ 172 timebins from the center. This peak is barely visible in figure 25 at an offset of ~ -172 timebins. To illustrate the difference in magnitude of the signal and the crosstalk, this zoomed in region was kept scaled to include the full crosstalk amplitude.

The digitizer card was operated at a sampling rate of 1.25 GHz, meaning it recorded the current output every 0.8 ns. This data was saved in batches of 2 GS (2 Gigasamples, so $2 \cdot 2^{30}$ samples) per channel, corresponding to $\sim 1.7\,\mathrm{s}$ of data per file. Unfortunately, the writing speed of the RAID used to store the data was only sufficient to achieve a duty cycle of $\sim 70\,\%$.

Figure 26 shows various views of a fully assembled MI²SO telescope inside the ECAP laboratory. Subfigure 26a shows the outside and top part of the telescope, including the scope of the guiding camera, Fresnel lens and cloth tubing. A view inside the telescope can be seen in subfigure 26b, showing the stabilization and anti-fogging measures taken behind the lens. Subfigure 26c shows the start of the signal line with the back of the PMT, gain control box and amplifier. Finally, the tubing extension to catch stray light and aluminium rods for wavelength-dependent focal length adjustment can be seen in subfigure 26d.

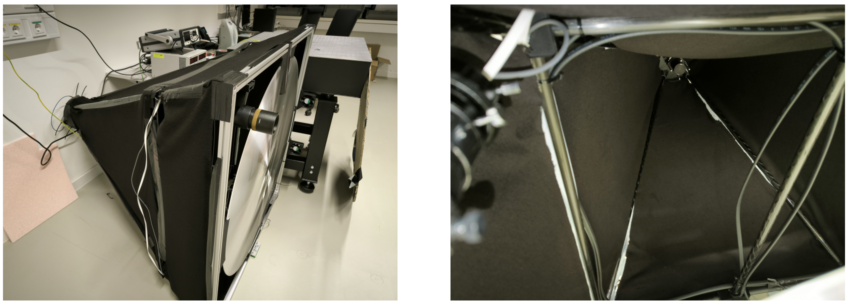

(a) A MI²SO telescope in the laboratory with guiding camera and cloth tubing visible.

(b) View inside a MI²SO telescope, exposing the secondary stabilization frame, heating cables and closed off optics and detector tubing.

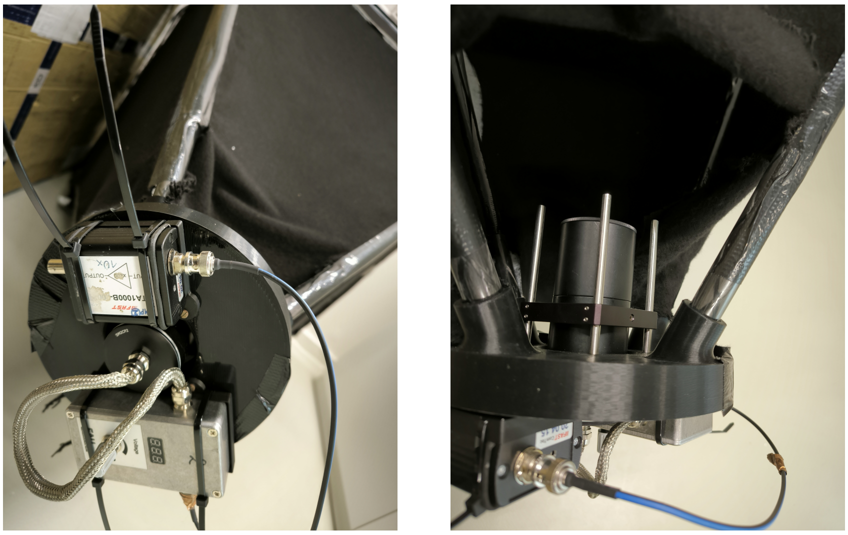

(c) PMT housing crown with PMT, gain control box and amplifier box.

(d) View inside the cloth tubing directly above the PMT housing crown, exposing the optics and detector tubing extension.

Figure 26: Four detail views of different parts of a MI²SO telescope.

3 Target selection and telescope setup

As was established in section 1.8, an intensity interferometer's performance given fixed electronic detection parameters is dependent on the target's flux. This necessitates the selection of suitable targets given the interferometer's collection area and geographic location. To remind ourselves of the derived signal-to-noise, once more equation 22:

$$S/N \propto A\alpha_{\mathrm{qe}}\alpha_{\mathrm{trans}}R_\star k_{\mathrm{A}}k_{\mathrm{s}}k_{\mathrm{pol}}F(\omega)\sqrt{\frac{T\Delta\omega}{2\sigma_{\mathrm{t}}}} \tag{25}$$

With $R_\star$ and T being the key factors examined in the search for optimal target stars. The following section will include simulations of potential observation targets at various times throughout the year. These simulations were started upon the completion of a first prototype version of MI^{2}SO in March, however weather and issues noticed in test observations leading to iterations on the initial design pushed the observation timeframe into the summer months.

3.1 Available measurement time of potential targets

On the Northern hemisphere - especially during the summer months - the list of bright stars is quite short. Furthermore, obscuration by clouds reduces the number of available nights significantly. From a list of bright stars in the Northern summer sky, observable hours with the sun at an altitude of $\leq -12^\circ$ (nautical darkness) and stars at an altitude of $\geq 20^\circ$ were calculated for the likely observation timeframe early summer 2024(see figure 27). The histogram represents a first selection cut from the list of brightest stars visible during the summer months from the Northern Hemisphere. Stars with too little potential observation time were excluded from further selection cuts.

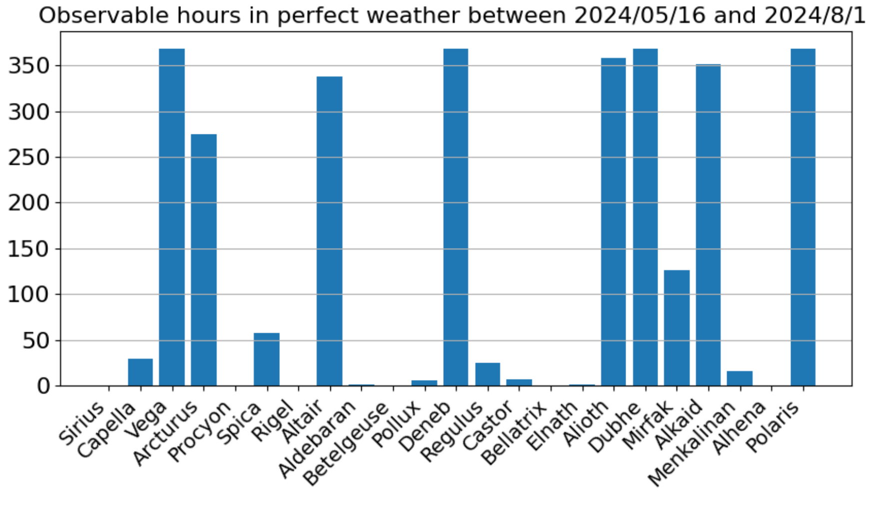

Figure 27: Histogram of hours spent above 20° observing altitude during nautical darkness of Northern night sky stars in early summer 2024.

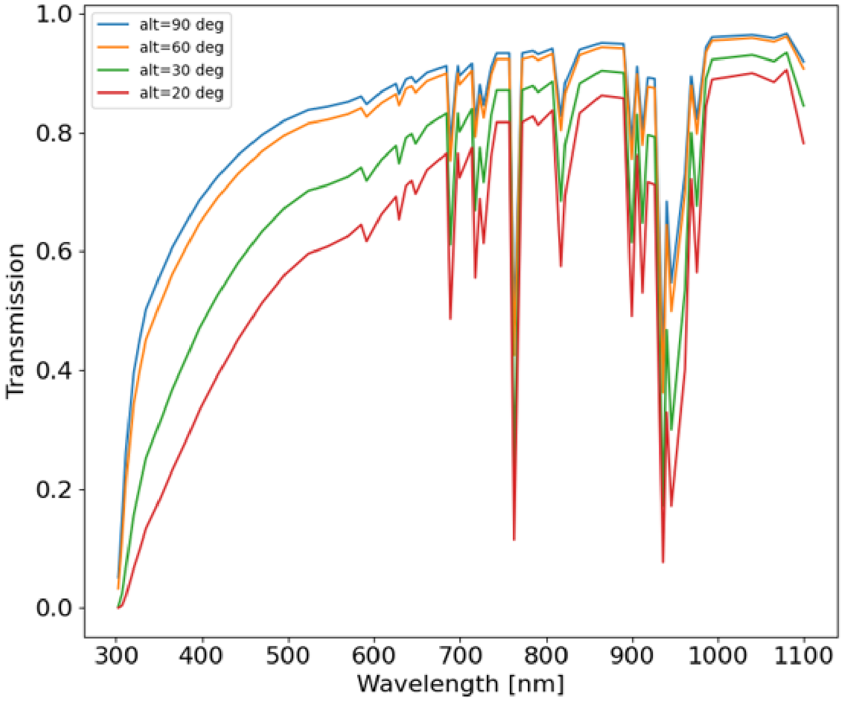

Figure 28: Atmospheric transmission vs wavelength at various altitudes above horizon. Long wavelengths at the edge of the optical spectrum and in the infrared show line absorption by the gases in Earth's atmosphere with the strength of the lines being proportional to the volume of air in the viewing direction dependent on altitude.

3.2 Expected photon rates and detection significance of potential targets

Observing a star at low altitude above the horizon puts more atmosphere into the path of light leading to more absorption. This effect is especially pronounced when observing at low wavelengths as illustrated in figure 28. Wavelength-dependent atmospheric transmission rate is modeled in the figure for various observation altitudes using the data from [40]. There is a clear trend visible of shorter wavelength light having weaker atmospheric transmission factors, especially at lower observation altitudes with more volume of atmosphere in the viewing direction. There are other contributing factors, such as atmospheric optical depth driven by local dust accumulation. To accurately model this effect, aerosol density near the telescopes would have to be measured due to the localized nature of it. Due to the lack of accurate, local aerosol density data, the atmospheric transmission as modeled in figure 28 was seen as a ”best case” of optimal observation conditions regarding aerosols impacting the atmosphere's optical depth. On at least one test measurement night, observation was impaired by Sahara dust, noticeable as a clear decrease in star photon rate compared to nights with the same instrumentation and similar pointing direction.

The strong effect of wavelength on atmospheric absorption led to different criteria for viable observing altitudes depending on each star's spectrum. Blue stars, especially ones that do not rise very far above the horizon during the summer, are much more strongly

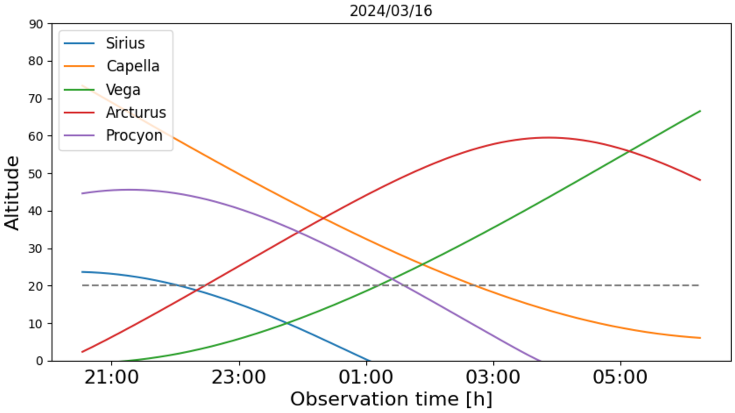

Figure 29: Paths of various blue and red stars during nautical darkness on March 16th. The dashed line indicates an altitude of 20 °, below which blue stars especially lose a significant amount of of intensity to atmospheric absorption.

affected by atmospheric absorption and this effect needs to be taken into account when deciding observation targets. Figure 29 illustrates the paths of various observation candidates during an example observation night. While Sirius, Vega and Procyon are blue stars significantly hotter than the Sun, Arcturus and Capella are colder than the Sun and peak in the red wavelengths.

One example for a blue star expected to be strongly affected by atmospheric absorption would be Sirius. Despite the large advantage over other stars in apparent magnitude, having a very low amount of available hours above 10 ° altitude (below which a treeline to the West of the roof makes observations impossible) and a high effective temperature ultimately led to it being excluded as a target. While the expected rates start out much higher than other stars, they decrease drastically over the already low amount of available hours.

Figure 30 shows a comparison for expected photon rates of Sirius, Vega and Arcturus in the night of March 31st. This date was chosen outside of the observation window in summer to include Sirius to further illustrate the altitude- and wavelength-dependent atmospheric absorption. Sirius already sets quite early in the night and is not visible from the Northern hemisphere in summer, but the effect of altitude-dependent atmospheric absorption on Sirius' blue light (effective temperature almost 4 times as high as of the sun) can be clearly seen in this plot. The calculations and factors taken into account for these expected rates are explained in later comparisons, this figure should illustrate the steep slope in expected rate resulting from atmospheric absorption when observing blue stars.

The critical points of comparison for potential observation targets are the available hours and the achieved significance n over an observation time T. When observing at a theoretical projected baseline of $b = 0$, this significance can be defined as [41]:

$$n = \sqrt{\frac{\lambda_0^4 R_\star^2 T}{4\sigma_t c^2 (\Delta\lambda)^2 (1 + \frac{R_{\text{NSB}}}{R_\star})^2}} \tag{26}$$

With filter center wavelength λ_0, star photon rate $R_\star(\lambda_0, \Delta\lambda)$, time resolution σ_t, filter width $\Delta\lambda$ and night sky background rate $R_{\text{NSB}}(\lambda_0, \Delta\lambda)$.

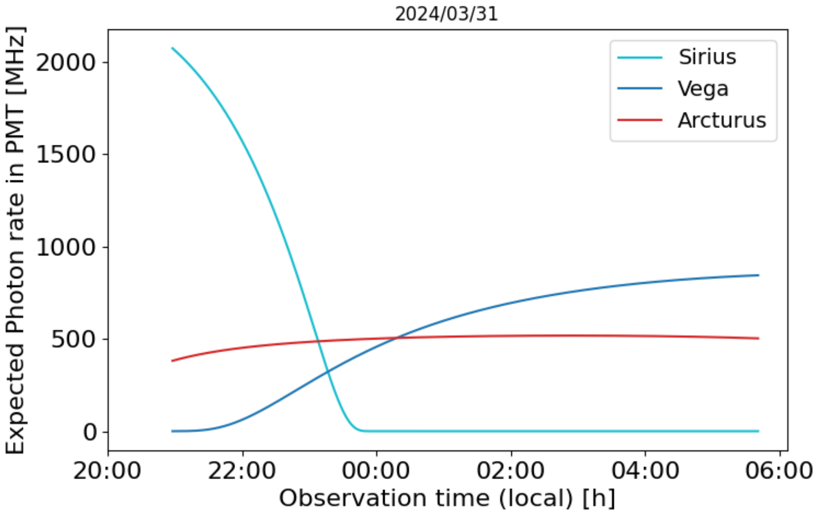

Figure 30: Comparison of expected photon rates for Sirius, Vega and Arcturus in the night of March 31st.

This equation illustrates the contribution of several key parameters of the instrument, such as time resolution σ_t or filter center wavelength λ_0, but it also contains the observed photon rate from the star (and night sky background). This rate $R_\star$ also needs to be estimated. First, the photon flux per unit area and wavelength was estimated with a blackbody model of each star's effective temperature and magnitude. This flux was then multiplied by the altitude-dependent atmospheric transmission factor calculated using the real altitudes of each star throughout the observation night in question. Finally, using the prospective optical filters' transmission profile as well as constant factors for lens transmission (manufacturer provided value), pinhole transmission and PMT detector efficiency (averaged over each filter's wavelength band from the manufacturer's datasheet) the expected photon rate, both average and at arbitrary time intervals during the observation night, could be calculated. Figure 31 shows the wavelength-dependent transmission profile of one of the candidate filters (SEM-FF02-655/40-25-D), calculated at a half cone angle of $22.6\,^\circ$, corresponding to the unfocused light cone from the $1\,\mathrm{m}$ diameter Fresnel lens at a distance of $f = 1.2\,\mathrm{m}$.

Using this expected photon rate, observations of the most viable candidates were simulated and achieved significances in one hour of observation time for each filter compared to ultimately decide whether a new filter should be ordered and which one.

Figure 32 shows one of the comparisons done for red stars cooler than the sun. Arcturus being the highest photon rate candidate among these predestined it as the target to compare candidate filters for. As can be seen in the plot, the filter SEM-FF02-655/40-25-D, a Semrock bandfilter with center wavelength $\lambda_0 = 655\,\mathrm{nm}$ and width of $\Delta\lambda = 47\,\mathrm{nm}$ performed the best for Arcturus observations. Its transmission profile was already mentioned and illustrated in figure 31.

With the different filters for different wavelength bands decided, comparisons of achieved significance between potential targets marked the next step. Using the expected photon rates based on simulated star spectra, atmospheric absorption based on each star's path in the sky, filter transmission and quantum efficiency with the filters and PMTs in

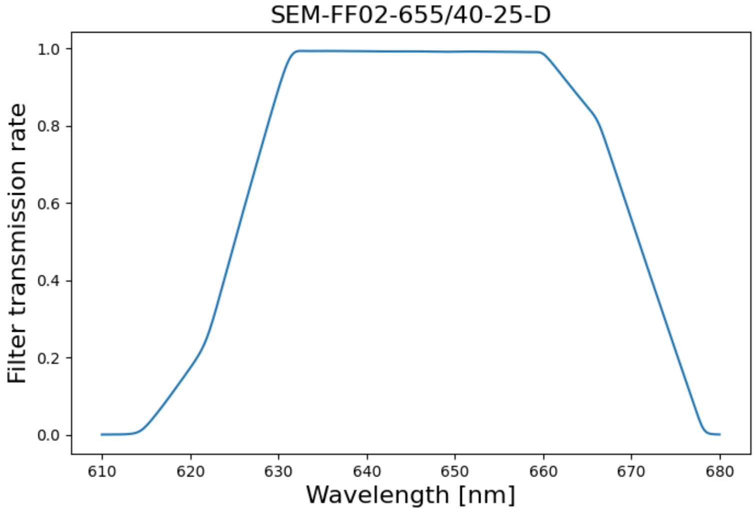

Figure 31: Transmission profile of SEM-FF02-655/40-25-D filter for half cone angle of 22.6 °. This transmission profile was generated using the manufacturer's online tool 'MyLight' [42].

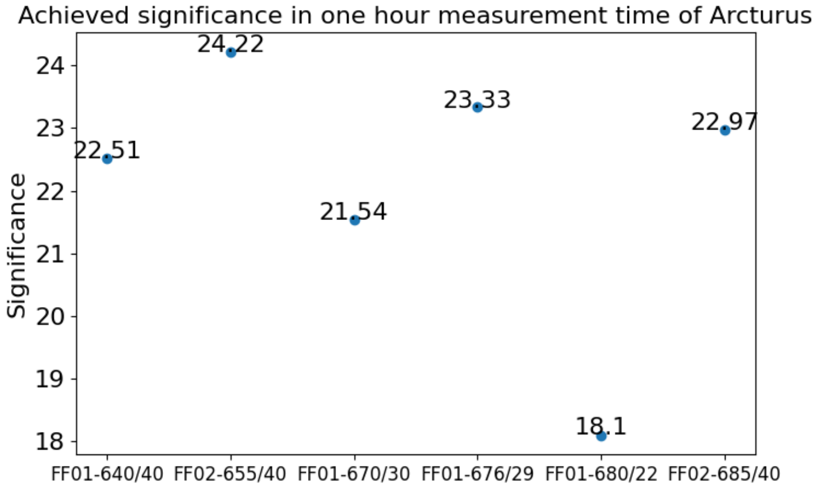

Figure 32: Comparison of various candidate filters for red star observations.

use, each promising observation night with little to no cloud cover was simulated and evaluated.
Figure 33 shows a rate comparison for Arcturus and Vega for a potential observation night mid June. The expected achieved significance over the observation night via equation 26 for these two stars was almost equivalent at $n_{\text{Vega}} \approx 42.1$ and $n_{\text{Arcturus}} \approx 42.7$. Despite the higher photon rate for Vega, Arcturus achieves comparable or better significance in simulations, highlighting the strong dependence on wavelength λ_0 already visible in equation 26. These values represent the highest achieved values across different available filters. A switch in the optical filter within one observation night would

result in significant loss due to refocusing at a different focal length, so it was deemed impractical. Observing Arcturus with the blue filter that produced $n_{\text{Vega}} \approx 42.1$ in simulations results in a much larger loss of photon rate (and therefore significance) than observing Vega with the red filter optimal for Arcturus. Finally, Arcturus starts to set earlier and earlier during the summer months, leading to the conclusion of observing Arcturus until it sets and Vega afterwards in each observation night, both using the red filter.

Due to several factors in the rate calculation being manufacturer provided values for the single components' manufacturing run, it was not expected to achieve precisely the $R_\star$ calculated here, but instead it was used to estimate losses from factors such as degradation or fogging of the lens, filter and PMT as well as obscuration by the telescope's stabilizing frame and heating cable.

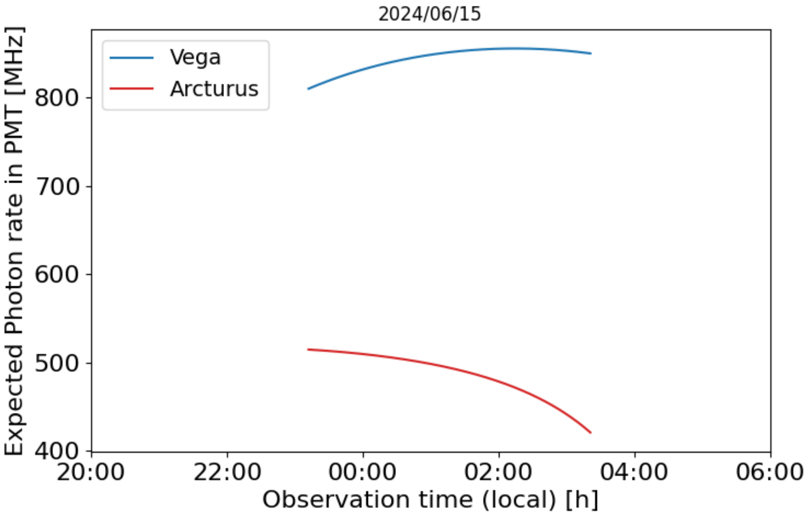

Figure 33: Photon rate comparison for Vega and Arcturus in the night of June 15th.

3.3 Relative telescope positions

When doing II with large collection area telescopes, one is often very limited, if not fully locked into one set of relative telescope positions. This does not result in only one possible baseline per telescope pair because of the Earth's rotation. However, mobile telescopes allow adjusting these relative positions to optimize several factors. Firstly, due to the significantly longer required observation time to achieve good statistics, telescopes should be positioned in a way that minimizes the change in projected baseline over one measurement Δb to reduce this uncertainty factor.

Figure 34 illustrates the effect of different telescope arrangements on Δb over the course of a night. These baseline calculations were subsequently converted to expected spatial coherence based on literature values for the angular diameter of the two stars. Using this expected spatial coherence, simulations were then carried out to determine the optimal relative telescope positions.

This was achieved by simulating the chosen observation target's path throughout the

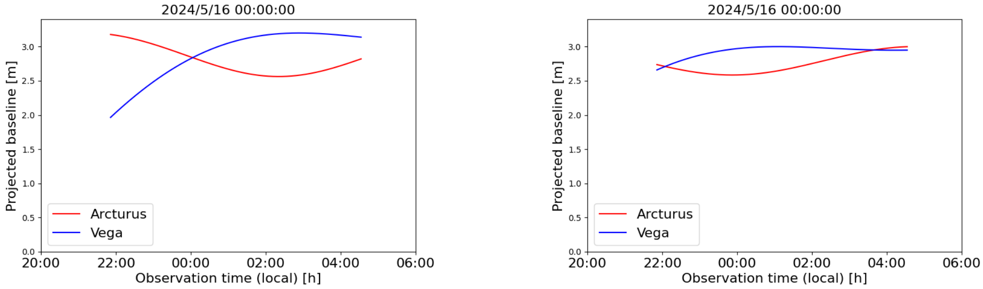

(a) Projected baseline over the course of an observation night for Vega and Arcturus with high baseline variance.

(b) Projected baseline over the course of an observation night for Vega and Arcturus with low baseline variance.

Figure 34: Projected baseline over the course of an observation night for Vega and Arcturus with different relative telescope positions.

observation night and calculating the projected baseline using a wide range of possible telescope arrangements (3–9 m physical distance between the telescopes and 0–360 ° angle relative to the meridian, see figure 35). The telescopes were finally arranged at an angle for which high spatial coherence and low Δb was simulated. This was the case at 30 ° relative to the meridian, slightly north of east-northeast.

The figure 35 only shows the simulation for Arcturus. Because Arcturus was determined as the primary observation target, telescope positions were optimized for Arcturus observations first and foremost. Furthermore, due to Vega's significantly smaller angular diameter (factor of ~ 7) compared to Arcturus, the expected spatial coherence for Vega varies significantly less over the same range of projected baselines.

Figure 36 shows the effect of Vega's comparatively small size on expected spatial coherence — projected baselines to the order of 15 m would be necessary to see a significant change in coherence. The telescope configuration used for this simulation is the same as in subfigure 34a, illustrating that despite a larger variance in projected baseline, the expected spatial coherence for Vega remains near perfectly constant while the same factor visibly varies for Arcturus over the course of the observation night.

Due to our knowledge of the spatial coherence function's shape, it is not necessary to measure precisely at which projected baseline coherence reaches zero. In fact - it could be counterproductive due to the difficulty of gathering good statistics at vanishingly low spatial coherence due to its effect on signal-to-noise ratio. Instead of searching for the zero coherence point, telescopes were arranged (using the same projected baseline calculation used for the angle) at distances that allowed for measurements at projected baselines b_i further apart than Δb. The lowest b_i was chosen to be at least Δb higher than the expected point of zero coherence while the highest b_i was chosen in a way that prevents the telescopes from touching as well as casting a shadow on each other. The predetermined telescope arrangements were then used for two observation nights each in order of decreasing b_i.

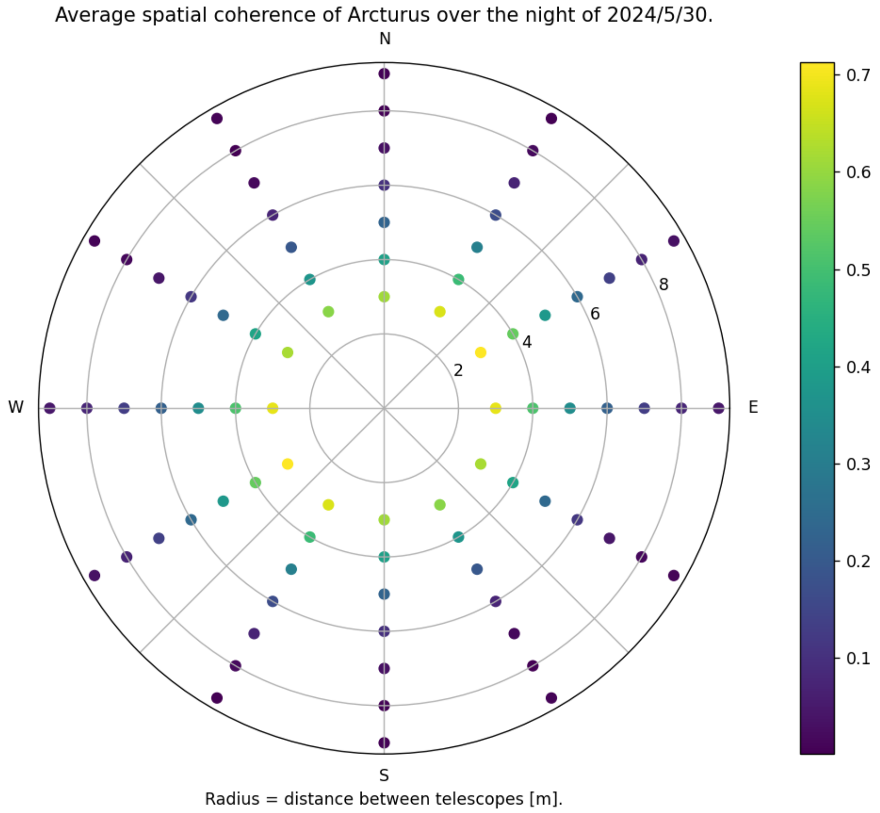

Figure 35: Expected average spatial coherence in color gradient over an observation night with telescope 1 in the center and telescope 2 at various positions on a compass coordinate system. Concentric circles indicate 2, 4, 6, and 8 m physical distance between the telescopes used to calculate projected baseline and spatial coherence.

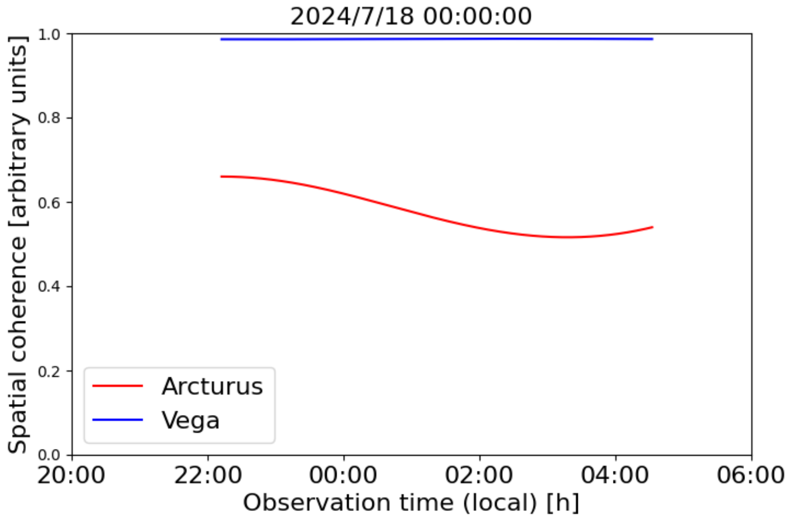

Figure 36: Expected spatial coherence over the course of an observation night for Vega and Arcturus in one possible telescope configuration.

4 Measurement results

After some test measurements and final adjustments to the telescope design and measurement electronics, Arcturus and Vega were measured at two different relative telescope positions in four nights in July. Measurements were aimed to start as soon as the night sky was dark enough to achieve stable tracking on Arcturus and were continued until the star reached an elevation of $\sim 9.5\,^\circ$, at which point it sets below the crowns of a treeline to the West of the ECAP roof. Vega observations were commenced after Arcturus sets each night. Calibration files measuring the offset in photocurrent without any events and average single photon pulse shape and area are recorded each night.
All of the data analysis and several parts of the instrument control discussed in the following chapter was done via *python* scripts. Most of these scripts were adapted from similar scripts used in H.E.S.S. II measurements [20], adjusted to work with the MI^{2}SO telescope geometries and faster sampling rate. The analysis script used in section 4.1.3 was written specifically for this work.
In one of the nights, the sampling rate of the digitizer card was set to 625 MHz for one hour to test whether data at different sampling rates could be combined and analyzed together. Aliasing problems in this data led to it being excluded from the analysis. This exclusion results in a total of 5200 files from the 18th of July, 2507 from the 28th, 4476 from the 29th and 6000 from the 30th, respectively. In total, with each file containing 2 GS taken at 1.25 GHz, this amounts to 8 hours and 40 minutes of data.
On the 18th and 28th of July, the telescopes stood separated by 3.2 m at an angle of $55\,^\circ$ NNE. On the 29th and 30th of July, the telescopes stood separated by 4.85 m at the same angle.

In two of the observation nights, one file was recorded with the telescopes pointed off the star (in azimuth, to preserve altitude-dependent effects) to determine night-sky background count rate R_{NSB}. This rate — even with a bright moon — only reached

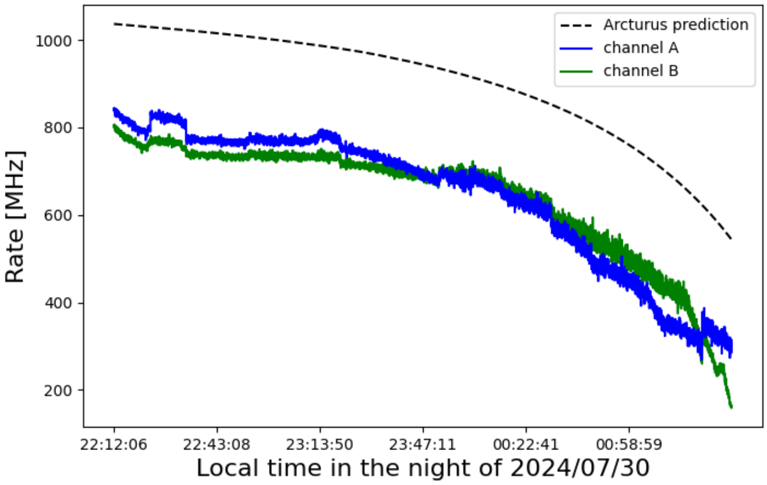

Figure 37: Photon count rates in both telescopes compared to prediction. The effects of thin clouds can be seen as well as the star setting below the treeline earlier in channel B than in channel A.

20–30 MHz, while the count rate on target in some cases exceeded 1 GHz. Figure 37 shows the count rates in both telescopes relative to the simulation script mentioned in section 3.2 for one of the observation nights. The simulation script assumes perfect atmospheric conditions, nominal performance of all electronics as well as no optical losses due to a degraded lens, slight off-focus position or reduced transmittance of the filter. As can be seen in figure 37, the measured count rates consistently lie at $\sim 80\,\%$ of the predicted rates, indicating some minor losses.

Data was correlated offline after the observation nights. This step converted the two channel photocurrent-sampling data (translatable to count rates using calibration files for photocurrent offset and average single photon peak shape and area) to an unnormalized $g^{(2)}(r_1, r_2, 0)$ for each data file. Figure 38 shows an example of such a file.

Measurement "chunks" were then defined as full night datasets and in the case of the 29th and 30th of July, a combined dataset of two nights. Chunking data into smaller acquisition time periods was deemed too detrimental for the statistics of the signal. Using these defined chunks, measured $g^{(2)}(r_1, r_2, 0)$ was averaged over the chunk (with each file weighted by the product of photon rates in each channel) and several filters applied. The sampling rate of the digitizer card introduces a pattern into the data, which is also corrected for in this step. To this end, the pattern correction used in H.E.S.S. data analysis [20] was used, but reconfigured to account for the doubled sampling rate used in MI²SO observations. A digital low-pass (cutoff frequency of 200 MHz) was applied as well as multiple notch filters set to noise frequencies standing out in the Fourier spectrum of multiple randomly selected single files as well as the Fourier spectrum of the chunk. Notch filters selectively suppress a band of frequencies around a center frequency, strength and width of this suppression being variable through their parameters. To examine both single files as well as full normalized $g^{(2)}$ functions for a measurement chunk for noise frequencies, a Fast Fourier Transform (FFT) of sample single files and each measurement chunk was calculated. As already demonstrated in figure 23, the analog low-pass filter was not expected to be sufficient in reducing

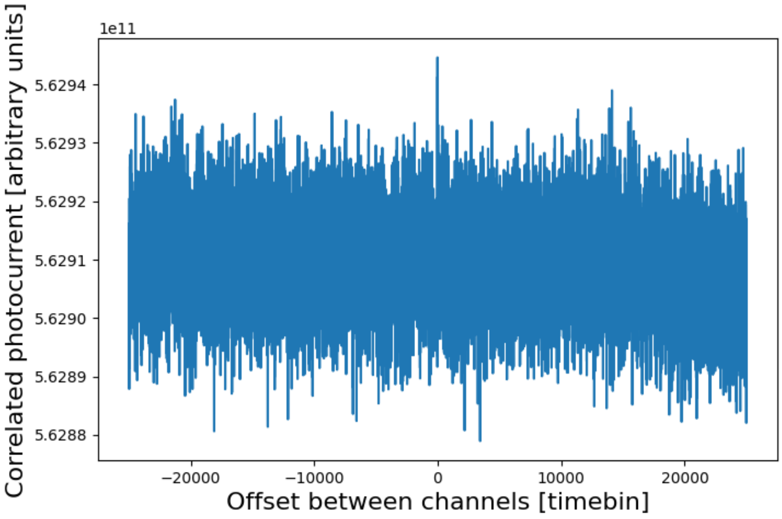

Figure 38: Unnormalized correlated photocurrent for one measurement file of 2 GS per channel.

high-frequency noise. An example for this averaged measured $g^{(2)}(r_1, r_2, 0)$ was shown in figure 24 and 25. Figure 39 shows the region of interest around the expected photon bunching peak position before and after applying notch filters at two radio broadcast frequencies that showed significant noise contribution in several observation nights.

Figure 40 illustrates the effects of various correction methods applied to the data. The first approximation for the expected signal was calculated by generating the FFT of the two channels' correlated average single photon pulse shape from calibration data. The

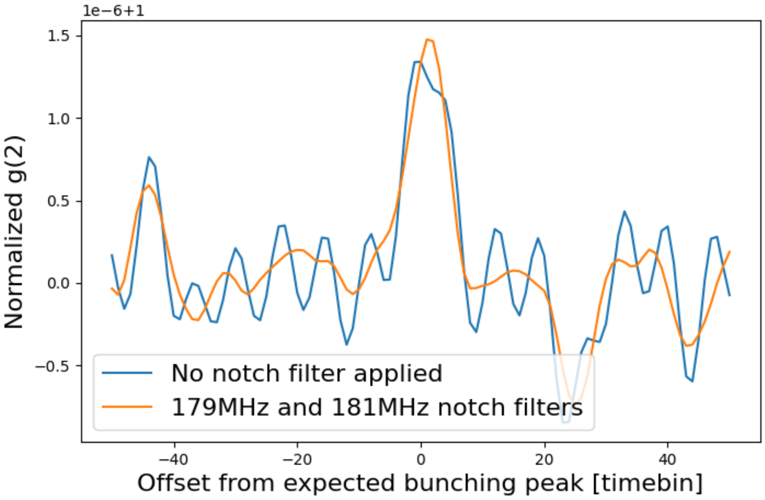

Figure 39: Normalized measured $g^{(2)}$ for one measurement chunk at different stages of filter application.

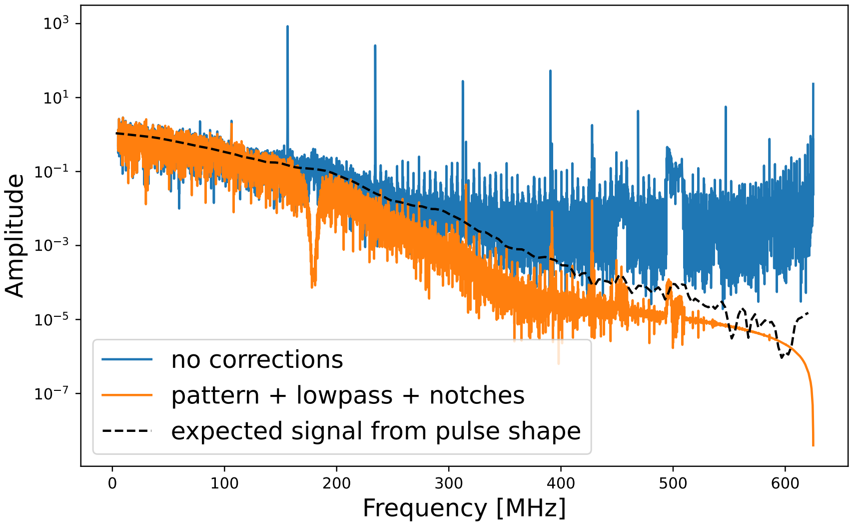

Figure 40: FFT of one observation night's full dataset $g^{(2)}$ function without any corrections (blue) and with pattern correction, digital low-pass filter and known noise frequency notch filters applied (orange). The black dashed line shows a first approximation of the expected signal.

pattern in the data resulting from the digitizer card's sampling rate can be seen as clear peaks at 78.125 MHz with harmonics. The amplitude of these peaks in the FFT reaches almost 10^3. The orange curve shows the most prominent peaks at 156.25 , 234.375 and the smaller peak at the fundamental frequency of 78.125 MHz fully vanishing, for higher harmonics the pattern correction still results in a significant reduction in amplitude, but does not fully take care of this pattern. The low-pass filter applied has a cutoff frequency of 200 MHz, which is where the blue and orange curves in the figure start to diverge visibly. Finally, the effect of the notch filters can be seen around 180 MHz in the V shape of the orange curve. The data for several nights showed significant correlated noise resulting from DAB+ radio frequencies at 179 and 181 MHz. The parameters of the notch filter (width and quality factor) applied were kept the same across different observation nights, resulting in potentially an overcorrection for observation nights with relatively lower noise contribution in these bands, such as the example night chosen here. Finally, a lot of distinct noise peaks and broader noise bands can be seen in higher frequencies. These frequencies were generally seen as sufficiently suppressed by the combination of analog and digital low-pass filters, however, further examination on the parameters of the digital low-pass filter and their effect on data quality could help optimize this correction. Finally, around 500 MHz the blue curve shows two wider bands of noise that are suppressed in the orange curve by the low-pass filter. These bands are two TV broadcast frequency bands of 8 MHz width each.

The projected baseline between the two telescopes varies over the course of a night due to Earth's rotation and its path around the sun. However, due to the 29th and 30th of July being consecutive nights, the variance in projected baseline over one night is only marginally smaller than the variance over both nights combined. Because the telescopes were positioned further apart, the (expected to be) reduced spatial coherence of the target from longer projected baselines would reduce the signal strength. To compensate for this effect, data from both nights was combined and analyzed as a single datapoint to achieve similar statistics to the observation nights at shorter telescope distance.

4.1 Photon bunching peak fitting — Arcturus data

The photon bunching peaks in the correlated data were analyzed using three different approaches to the time resolution and expected peak shape. The approach with the least assumptions is the "unfixed σ" approach. In the "HESS–fixed σ" approach, the peak width was determined using the combination of all datasets. Finally, in the "calibration peakshape" approach, measurements of the TTS were used to predict the photon bunching peak's shape.

4.1.1 Unfixed σ method

The photon bunching peak was fit using a Gaussian of the form $A \cdot \mathrm{e}^{\frac{-(x-\mu)^2}{2\cdot\sigma^2}} + d$ with A, μ, σ and d as free parameters. The peak position μ was constrained to be within 5 timebins of the predicted peak position calculated from the cable length difference and signal speed inside the cables used. Integrating over this Gaussian fit provides the coherence time observed in the analyzed dataset. As a gauge for the uncertainty of this coherence time, the fit function was added on top of the $g^{(2)}$ function at 200 different time differences between the telescopes (excluding the crosstalk region) to determine the variance of the integral if the photon bunching peak lay at different positions within the background noise. For the re-fit at different positions, σ was no longer left as a free parameter, but instead fixed to the original position's fit parameter result. Figure 41 shows a 100 ns window around the predicted peak position for the three measurement chunks with photon bunching peak fits. In this figure, the $g^{(2)}$ functions were offset on the y-axis to separate them visually.

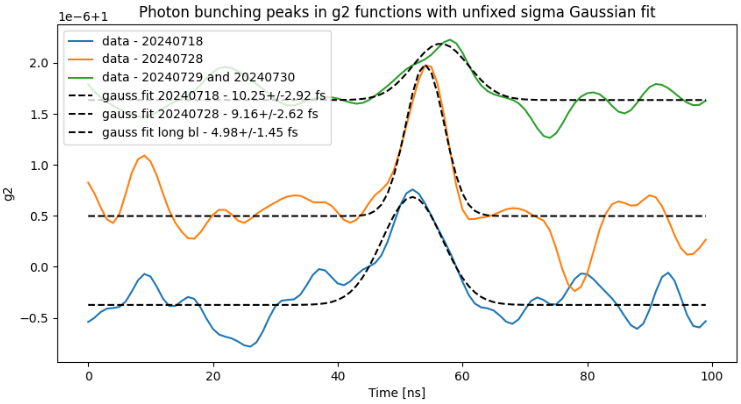

Figure 41: Photon bunching peaks in $g^{(2)}$ functions for all measurements chunks fitted with unfixed σ Gaussian. $g^{(2)}$ functions of each dataset were offset for illustration purposes.

4.1.2 HESS–fixed σ method

Because the time resolution of the instrument is orders of magnitude larger than the coherence time of light from the target, the width of the photon bunching peak should be dominated by instrument variables. Thus, this width (represented by the fit parameter σ in a Gaussian fit) should be constant across measurements of different stars and even different measurement campaigns so long as the time resolution of the instrument did not significantly change between campaigns from instrument upgrades or similar adjustments. In H.E.S.S. II data analysis [20], this σ is fixed to a constant value by combining all datasets of all stars with justified equivalent time resolution assumptions and fitting on this combined $g^{(2)}$.

MI^{2}SO does not have a large catalog of datasets to apply this method to, nevertheless the assumption of unchanged time resolution stands justified by the lack of instrument changes between the four nights in July. Therefore, data from these four nights was combined and a fixed value for σ determined.

Figure 42 shows the region of interest around the expected photon bunching peak in the combined $g^{(2)}$ of the four nights. A Gaussian fit using an *unfixed* σ in this combined dataset determines the fixed σ to be used when analyzing individual measurement chunks. The more data is taken by an instrument, the more accurate this gauge becomes for the time resolution of the instrument and its effect on photon bunching peaks. Figure 43 shows the fitted bunching peaks in the same way as in section 4.1.1.

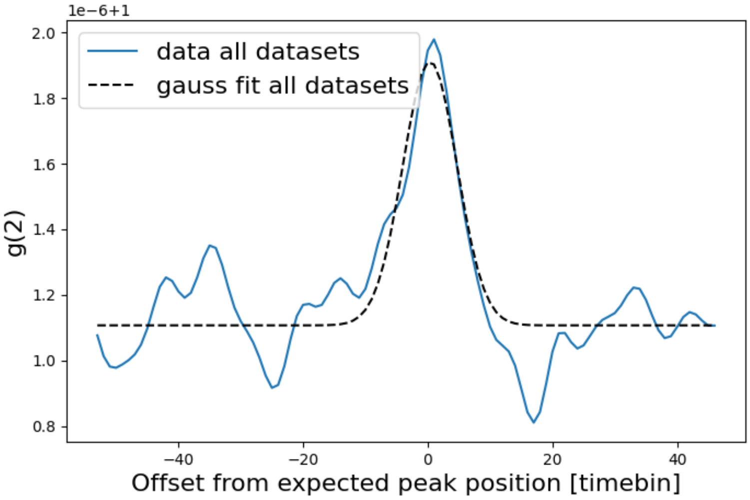

Figure 42: Photon bunching peak with Gaussian fit in combined $g^{(2)}$ of all July measurement chunks.

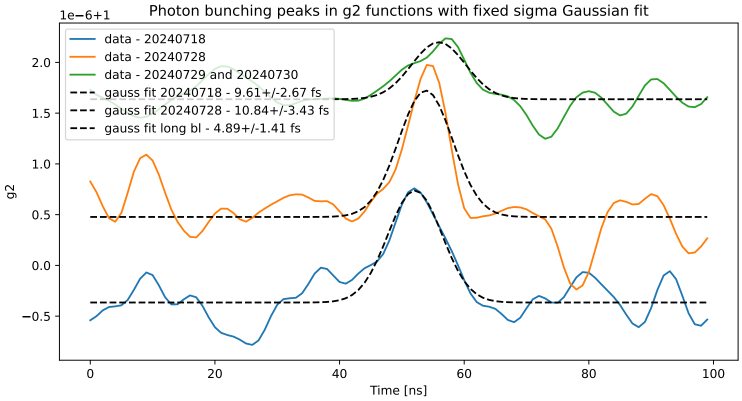

Figure 43: Photon bunching peaks in $g^{(2)}$ functions for all measurements chunks fitted with fixed σ Gaussian. $g^{(2)}$ functions of each dataset were slightly offset for illustration purposes.

4.1.3 Calibration peakshape method

Finally, the calibration peakshape method tries to approximate or predict the shape of a photon bunching peak using knowledge of the shape of single photon peaks in each channel as well as the TTS of the detectors. A photon bunching peak is assumed to have the same shape as the correlation of each detector's single photon peak, smeared by a Gaussian the width of its TTS. The average (determined over 100 events) shape of single photon peaks in each detector was extracted from the calibration file of each night. This average shape was subsequently broadened by a Gaussian $e^{\frac{-t^2}{2\cdot\sigma^2}}$ using

$\mathrm{TTS}_{\mathrm{FWHM}} = 2\sqrt{2\ln 2}\sigma$ with value for TTS measured in [34] for the control voltages used in each observation night on the detectors. For all measurements, the time resolution used was $\mathrm{TTS}_{\mathrm{FWHM}} = 0.75\,\mathrm{ns}$. In figure 44, one can already see the slight asymmetric shape of the expected peak. Furthermore, the swap in detection channels between the 18th and 28th of July is visible in aforementioned asymmetry. It can also be noted that the error on the size of the photon bunching peaks was smallest for the calibration peakshape method.

For all analysis methods, the photon bunching peak integral of each of the first two nights is significantly larger than that of the second two nights, during which the telescopes stood at longer distance from each other. This means MI²SO has detected Arcturus as a thermal lightsource of finite size, significantly changing in spatial coherence between baselines of $\sim 3\,\mathrm{m}$ and $\sim 4.3\,\mathrm{m}$.

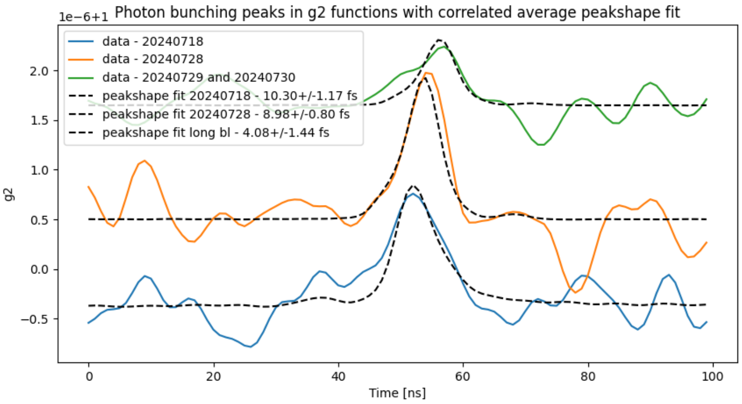

Figure 44: Photon bunching peaks in $g^{(2)}$ functions for all measurements chunks fitted with correlated TTS-smeared average single photon peakshape. $g^{(2)}$ functions of each dataset were slightly offset for illustration purposes.

4.2 Angular diameter of Arcturus

Using the coherence times determined by the three methods, the spatial coherence curve of Arcturus at $\lambda_0 = 655\,\mathrm{nm}$ can be fit using equation 24 with amplitude A and angular diameter θ as fit variables. Figures 45, 46 and 47 show this fit. The standard deviation in projected baseline over the duration of the measurement chunk was used as the x-error and shaded areas indicate standard error of the fit parameters A and θ. This resulted in values for the angular diameter of $\theta = 20.47 \pm 0.71\,\mathrm{mas}$, $\theta = 20.94 \pm 1.99\,\mathrm{mas}$ and $\theta = 22.97 \pm 1.74\,\mathrm{mas}$ for unfixed σ, HESS–fixed σ and calibration peakshape method, respectively. These values are in relatively good agreement with each other and their weighted average of $20.84 \pm 0.63\,\mathrm{mas}$ within $5.5\,\%$ of the literature value of $\theta = 19.77 \pm 0.05\,\mathrm{mas}$ [43]. The literature value listed here reflects the 700 nm value obtained with a uniform disk model in the cited paper. Because MI²SO was operated at 655 nm and a uniform disk model was used to determine the angular diameter, this value was chosen as a comparison over more recently determined limb-darkening model diameters in meta analyses of many observations across different instruments in [44].

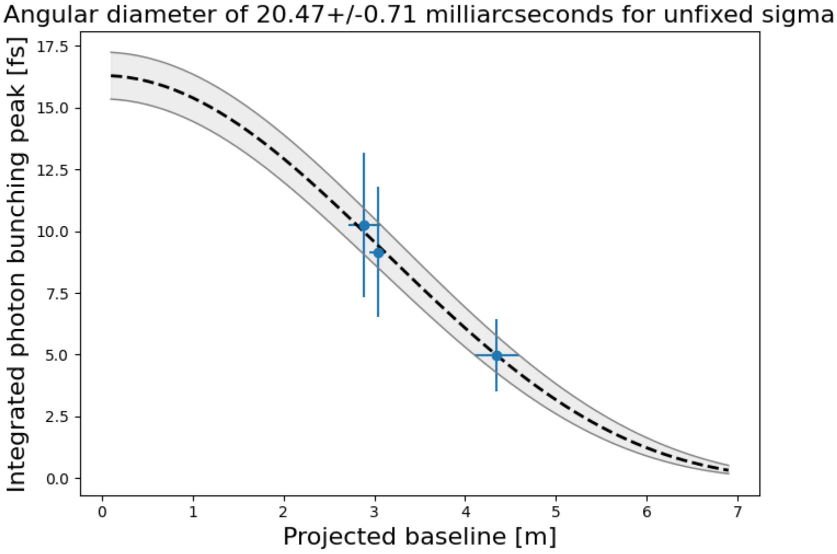

Figure 45: Spatial coherence curve fit for Arcturus using unfixed σ method.

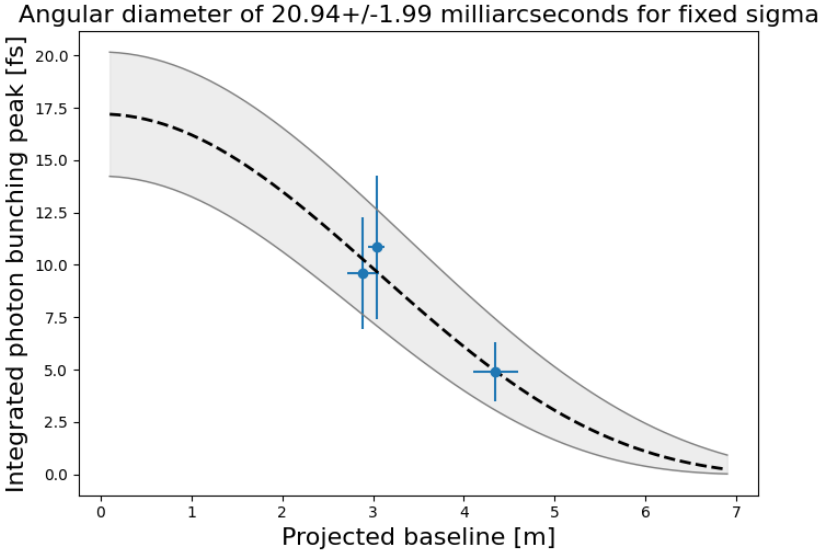

Figure 46: Spatial coherence curve fit for Arcturus using HESS–fixed σ method.

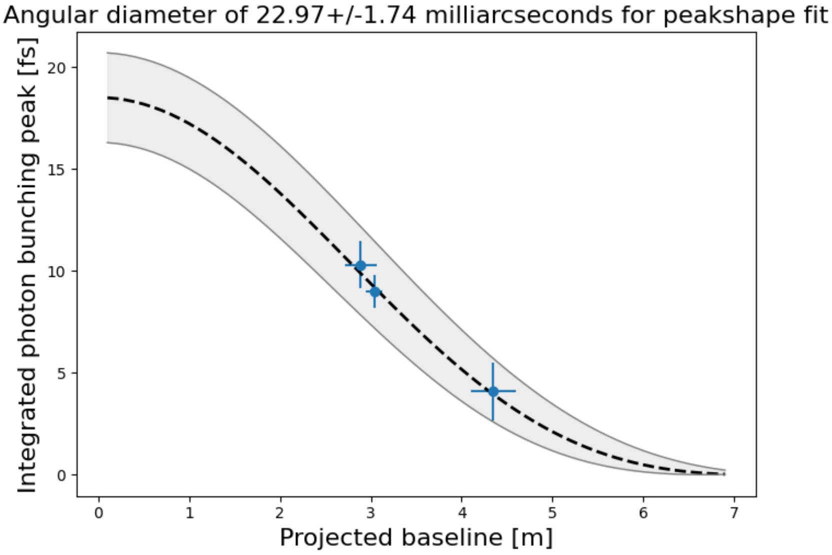

Figure 47: Spatial coherence curve fit for Arcturus using calibration peakshape method.

4.3 Vega measurements

In each observation night, Vega was observed after Arcturus observations had concluded until the sky was deemed too bright to continue observations. This typically was the case at the latest at civil twilight (with the sun at $-6\,^\circ$ below the horizon), at which point R_{NSB} reached levels comparable to $R_\star$. Vega is significantly less luminous than Arcturus at long red wavelengths, with simulations typically placing it at $\sim 2/3$ of the photon rates of Arcturus if viewed in the used filter.

Measured rates of Vega generally did not reach $\sim 80\,\%$ of the expected count rates as in the case of Arcturus, however all Vega measurements were — to varying degrees — affected by clouds and/or lenses fogging up. One night's Vega dataset was discarded after noticing that more than a third of the photon rate in the detectors was due to the ECAP building's stairwell lighting being reflected by the inner walls up unto the fogged up lenses. Due to diffuse light reflected from below the telescope having such a large effect on photon rates, the dataset was deemed unlikely to represent Vega accurately.

Due to the limited amount and lower quality (due to rate and the aforementioned noise factors) of Vega data, measurements were chunked together for each relative telescope position setup, resulting in just two datasets. Even after combining datasets of two nights, fitting the photon bunching peak proved difficult and only low statistics were achieved.

Figure 48 shows the $g^{(2)}$ functions for the two datasets, offset on the y-axis to separate them visually. From the figure it is already apparent that especially the data for the short baseline is of very low statistics. At the shorter distance between the telescopes, a coherence time of $10.23 \pm 6.34\,\mathrm{fs}$ was extracted using the HESS–fixed σ method, at the longer distance between them the result was $7.34 \pm 2.71\,\mathrm{fs}$. The uncertainty in peak area obtained via the unfixed σ method was larger than the peak areas for both datasets. The calibration peakshape method ran into this same problem for the short baseline dataset (blue in figure 48). The results for the HESS–fixed σ method lie close together, which is not unexpected. The projected baseline at which Vega's spatial coherence is expected to fall to its first minimum lies at a value eight times as high as for Arcturus. Because the distances between the telescopes were chosen to optimize for Arcturus observations, they do not differ enough to expect any significant change in observed spatial coherence for Vega.

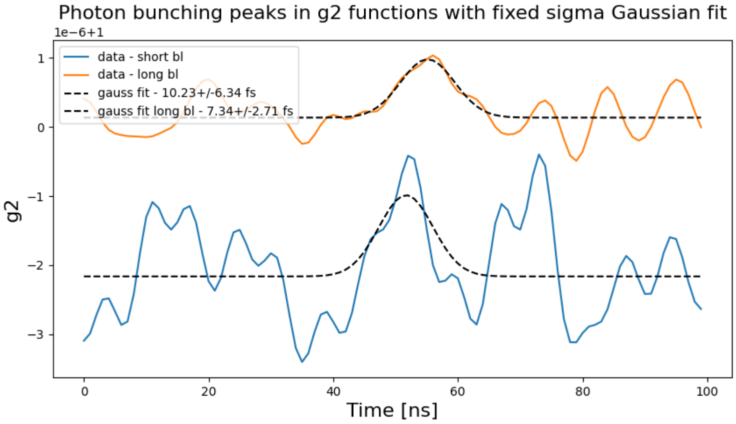

Figure 48: Photon bunching peaks in $g^{(2)}$ functions for the two measurement chunks of Vega data, fitted with fixed σ Gaussian. $g^{(2)}$ functions of each dataset were offset for illustration purposes

5 Summary and Outlook

Within the scope of this thesis, an intensity interferometer using Fresnel lenses was designed, constructed and its operation tested. Due to current projects in intensity interferometry often being conducted during off-cycle times of other instruments not primarily designed as interferometers (or intensity detectors) such as IACTs, the viability of dedicated low-cost instrumentation for the purpose of II was investigated.

Using Fresnel lenses presents a compromise in optical quality a dedicated intensity interferometer can easily make in order to drastically reduce both cost and weight relative to classical lenses or mirror dishes of similar lens speed and aperture size. The same goal of minimizing weight was applied to the lens frame and telescope structure, constructing it from aluminium, 3D-printed PLA-plastic of low fill factor and carbon fiber rods. Furthermore, emphasis was placed on using either standardized parts such as the aluminium profiles and tubing system or designing 3D-printed parts to interface between components of the telescope to facilitate a fast completion of prototypes and further versions of the telescope, addressing issues as they arise.

Determining the used lenses' point spread function presented an important step in the design process, limiting the potential detector choices to ones with detection surface area sufficient to capture the light focused by the lenses. To this end, a test setup using two optical benches was constructed and an automated measuring process scripted to examine the point spread function and potential deviations over time due to the light source's variability. This measurement determined the choice of Photo Multiplier Tube used in the telescopes.

The used PMTs' detection efficiency at different wavelengths presented a limiting factor on both optical filters and observable targets. Simulations were written and used to evaluate potential targets as to their potential for significant detection given a possible observation timeframe dictated by the completion of the telescopes. Observations were carried out as weather permitted on a limited list of targets determined to have the highest potential for detecting photon bunching peaks.

Using data from four nights amounting to just under 9 h, photon bunching peaks were detected and analyzed to determine the angular diameter of the star observed. Despite the low optical quality of Fresnel lenses, the lack of parallelization of the light beam to improve filter performance, relatively modest electronics dominating the time resolution and a low amount of data, the angular diameter of Arcturus measured with MI^{2}SO agrees with literature values to within 5.5 %. This demonstrates strong potential for even low-cost dedicated intensity interferometers to complement "borrowed instrument" II data.

Key drawbacks of small aperture size intensity interferometers have become apparent in this work in the low signal-to-noise ratio for fainter stars as well as the susceptibility to correlated electronic noise. These drawbacks can be worked around by having dedicated instruments to increase available measurement time and introducing filters combating the more egregious noise frequencies. One key advantage of small aperture size intensity interferometers could not be demonstrated in this work, but presents a clear role such instruments could play in high angular resolution astronomy: While a single star's spatial coherence curve follows the first order Bessel function, the majority of stars are found in binary or higher multiple systems. The spatial coherence curve of a multiple system contains variations on certain projected baseline intervals corresponding to the separation of the multiple stars. Because this separation is larger than the diameter of the stars for most inclination angles of a system when viewed from Earth, the signature of the separation in the spatial coherence curve is visible in variations within smaller projected baseline differences than the fall to the first minimum. When using IACTs, the single telescopes' large apertures average the projected baseline over a significant range determined by the diameter of the telescope. An intensity interferometer with one ”pixel” per telescope cannot determine whether a coincident photon pair impacted the two telescopes in each telescope's center, on two points closer together than the telescope centers by up to the sum of the two telescope radii, or two points further apart by that same amount. This uncertainty in projected baseline at which a target is observed makes intensity interferometers less sensitive to larger scale structures (such as the separation between two stars in a binary) the larger their aperture size. Small aperture size telescopes, such as dedicated Fresnel lens telescopes, could therefore be used to complement IACT II data. Using the high statistics knowledge gained from the large aperture telescopes on the spatial coherence curve ”envelope” of the intensity-dominant component of the system, small aperture telescopes could probe the spatial coherence on small projected baseline differences to assist with binary studies.

Another large advantage of MI^{2}SO lies in its low weight. Mobility already played a key role in Hanbury Brown and Twiss' success when developing the technique at the Narrabri Stellar Intensity Interferometer. By being able to move the telescopes, it was possible to measure spatial coherence at many different baselines for each target and optimize the choice of baselines for each target observed. The inclination angle of a binary system was already mentioned earlier regarding the relation between stars' diameters and their separation from each other. This inclination angle also determines the underlying structure in the spatial coherence curve on the u-v plane. When observing objects that are not circular, the spatial coherence curve can no longer be simplified to behavior over a one-dimensional projected baseline between the telescopes — the source geometry as well as each telescope pair's orientation relative to it determines what u-v coverage a pair of telescopes can bring. With mobile telescopes, advantageous orientations of the intensity interferometer relative to its target can be achieved and optimized for each target.

Lastly, increasing the amount N of telescopes of an intensity interferometer to $N + 1$ increases the amount of telescope pairs with data to be correlated by N rather than 1. This presents a possible way to address the signal-to-noise problem in intensity interferometers as well as widening u-v coverage in the case of binary systems. Key to taking advantage of this scaling would be low cost and complexity of the system to allow for fast assembly (or mobility). Specifically the scaling of an intensity interferometry array in quantity of telescopes and its effect on signal-to-noise requires further study as it could alleviate one of the core problems of the method.

Acronyms

ECAP Erlangen Center for Astroparticle Physics.

FFT Fast Fourier Transform.

H.E.S.S. High Energy Stereoscopic System.

HBT Hanbury Brown and Twiss.

IACT Imaging Air Cherenkov Telescope.

IACTs Imaging Air Cherenkov Telescopes.

II Intensity Interferometry.

MI^{2}SO Mobile Intensity Interferometer for Stellar Observations.

PMT Photo Multiplier Tube.

PMTs Photo Multiplier Tubes.

S/N signal-to-noise ratio.

TTS transit-time spread.

Bibliography

[1] R. HANBURY BROWN and R. Q. TWISS. "A Test of a New Type of Stellar Interferometer on Sirius". In: *Nature* 178.4541 (Nov. 1956), pp. 1046–1048. ISSN: 1476-4687. DOI: `10.1038/1781046a0`. URL: `https://doi.org/10.1038/1781046a0`.

[2] R. Hanbury Brown, J. Davis, and L. R. Allen. "The Angular Diameters of 32 Stars". In: *\mnras* 167 (Apr. 1974), pp. 121–136. DOI: `10.1093/mnras/167.1.121`.

[3] Mark Fox. *Quantum Optics: An Introduction.* Vol. 15. Oxford Master Series In Physics. New York: Oxford University Press, 2006, p. 13. ISBN: 978-0-19-856672-4.

[4] *The Rayleigh Criterion.* URL: `http://hyperphysics.phy-astr.gsu.edu/hbase/phyopt/Raylei.html` (visited on 11/24/2024).

[5] Mark Fox. *Quantum Optics: An Introduction.* Vol. 15. Oxford Master Series In Physics. New York: Oxford University Press, 2006, pp. 105–107. ISBN: 978-0-19-856672-4.

[6] *Mount Wilson Observatory | CHARA.* en-US. URL: `https://www.mtwilson.edu/chara/` (visited on 11/24/2024).

[7] Aaron Labdon. "The Inner Astronomical Unit of Protoplanetary Disks". PhD. University of Exeter, 2021. URL: `https://arxiv.org/abs/2111.06205` (visited on 11/24/2024).

[8] *Basics of Interferometry.* URL: `https://www.chara.gsu.edu/public/basics-of-interferometry` (visited on 11/24/2024).

[9] Mark Fox. *Quantum Optics: An Introduction.* Vol. 15. Oxford Master Series In Physics. New York: Oxford University Press, 2006, pp. 16–17. ISBN: 978-0-19-856672-4.

[10] Rodney Loudon and Larry Hunter. "The Quantum Theory of Light, Second Edition". In: *American Journal of Physics* 54.3 (Mar. 1986), p. 98. ISSN: 0002-9505. DOI: `10.1119/1.14652`. URL: `https://doi.org/10.1119/1.14652` (visited on 11/24/2024).

[11] Rodney Loudon and Larry Hunter. "The Quantum Theory of Light, Second Edition". In: *American Journal of Physics* 54.3 (Mar. 1986), p. 112. ISSN: 0002-9505. DOI: `10.1119/1.14652`. URL: `https://doi.org/10.1119/1.14652` (visited on 11/24/2024).

[12] Mark Fox. *Quantum Optics: An Introduction.* Vol. 15. Oxford Master Series In Physics. New York: Oxford University Press, 2006, p. 114. ISBN: 978-0-19-856672-4.

[13] Mark Fox. *Quantum Optics: An Introduction.* Vol. 15. Oxford Master Series In Physics. New York: Oxford University Press, 2006, p. 116. ISBN: 978-0-19-856672-4.

[14] Mark Fox. *Quantum Optics: An Introduction.* Vol. 15. Oxford Master Series In Physics. New York: Oxford University Press, 2006, pp. 117–119. ISBN: 978-0-19-856672-4.

[15] Rodney Loudon and Larry Hunter. "The Quantum Theory of Light, Second Edition". In: *American Journal of Physics* 54.3 (Mar. 1986), p. 111. ISSN: 0002-9505. DOI: `10.1119/1.14652`. URL: `https://doi.org/10.1119/1.14652` (visited on 11/24/2024).

[16] Dilleys Ferreira, Romain Bachelard, William Guerin, Robin Kaiser, and Mathilde Fouché. "Connecting field and intensity correlations: The Siegert relation and how to test it". In: *American Journal of Physics* 88.10 (Oct. 2020), 831–837. ISSN: 1943-2909. DOI: `10.1119/10.0001630`. URL: `http://dx.doi.org/10.1119/10.0001630`.

[17] Leonard Mandel and Emil Wolf. *Optical Coherence and Quantum Optics.* Cambridge: Cambridge University Press, 1995, pp. 188–191. ISBN: 978-0-521-41711-2. DOI: `10.1017/CBO9781139644105`. URL: `https://www.cambridge.org/core/product/F8CB94C70FA64CD3FB60890CA2048168`.

[18] Leonard Mandel and Emil Wolf. *Optical Coherence and Quantum Optics.* Cambridge: Cambridge University Press, 1995, p. 190. ISBN: 978-0-521-41711-2. DOI: `10.1017/CBO9781139644105`. URL: `https://www.cambridge.org/core/product/F8CB94C70FA64CD3FB60890CA2048168`.

[19] Leonard Mandel and Emil Wolf. *Optical Coherence and Quantum Optics.* Cambridge: Cambridge University Press, 1995, pp. 170–171. ISBN: 978-0-521-41711-2. DOI: `10.1017/CBO9781139644105`. URL: `https://www.cambridge.org/core/product/F8CB94C70FA64CD3FB60890CA2048168`.

[20] Andreas Zmija, Naomi Vogel, Frederik Wohlleben, Gisela Anton, et al. "First intensity interferometry measurements with the H.E.S.S. telescopes". In: *Monthly Notices of the Royal Astronomical Society* 527 (Feb. 2024). Publisher: OUP, pp. 12243–12252. ISSN: 0035-8711. DOI: `10.1093/mnras/stad3676`. URL: `https://ui.adsabs.harvard.edu/abs/2024MNRAS.52712243Z`.

[21] Mark Fox. *Quantum Optics: An Introduction.* Vol. 15. Oxford Master Series In Physics. New York: Oxford University Press, 2006, p. 106. ISBN: 978-0-19-856672-4.

[22] Andreas Zmija. "From the Lab to the Telescopes - Intensity Interferometry with H.E.S.S". PhD Thesis. Erlangen - Nuremberg U., 2024. DOI: `10.25593/open-fau-1153`.

[23] R. Hanbury Brown. *The intensity interferometer; its application to astronomy.* Journal Abbreviation: London Publication Title: London. Jan. 1974, p. 63. URL: `https://ui.adsabs.harvard.edu/abs/1974iiaa.book.....B`.

[24] Pko. *Comparison of Fresnel lens and normal lens.* 2006. URL: `https://commons.wikimedia.org/wiki/File:Fresnel_lens.svg` (visited on 11/24/2024).

[25] *H.E.S.S. - The High Energy Stereoscopic System.* URL: `https://www.mpi-hd.mpg.de/HESS/pages/about/HESS_I_II/` (visited on 11/24/2024).

[26] Basler. *acA2500-60uc | Basler Product Documentation.* URL: `https://docs.baslerweb.com/aca2500-60uc` (visited on 11/24/2024).

[27] Hans Michael Eichler. "Characterisation studies on the optics of the prototype flourescence telescope FAMOUS". MA thesis. Aachen: Rheinisch-Westfälische Technische Hochschule Aachen, 2014. URL: `https://web.physik.rwth-aachen.de/user/hebbeker/theses/eichler_master.pdf` (visited on 11/24/2024).

[28] Hamamatsu Photonics K.K. *Photomultiplier Tubes and Photomultiplier Tube Assemblies Hamamatsu R11265U series/H11934 series.* 2019. URL: `https://www.hamamatsu.com/content/dam/hamamatsu-photonics/sites/documents/99_SALES_LIBRARY/etd/R11265U_H11934_TPMH1336E.pdf` (visited on 11/24/2024).

[29] Hamamatsu Photonics K.K. *Photomultiplier Tubes and Photomultiplier Tube Assemblies Hamamatsu H15460 series/H15461 series.* 2023. URL: `https://www.hamamatsu.com/content/dam/hamamatsu-photonics/sites/documents/99_SALES_LIBRARY/etd/H15460_H15461_TPMO1096E.pdf` (visited on 11/24/2024).

[30] Sky-Watcher. *Skywatcher EQ8-R manual.* URL: `https://inter-static.skywatcher.com/downloads/eq8r_v4.pdf` (visited on 11/24/2024).

[31] Sky-Watcher. *Skywatcher EQ8 manual.* URL: `https://inter-static.skywatcher.com/downloads/eq8_221018v2.pdf` (visited on 11/24/2024).

[32] Starlight Xpress. *Starlight Xpress Lodestar Pro datasheet.* 2022. URL: `https://www.sxccd.com/wp-content/files/2022-SX-Autoguider-Specification.pdf` (visited on 11/24/2024).

[33] Starlight Xpress. *Starlight Xpress Lodestar X2 Handbook Manual.* 2014. URL: `https://www.manualslib.com/manual/1574976/Starlight-Xpress-Lodestar-X2.html` (visited on 11/24/2024).

[34] Paul Blaß. "Charakterisierung von Photomultipliertubes für die zukünftige Anwendung in der Intensitätsinterferometrie". German. BSc Thesis. Erlangen: Friedrich-Alexander-Universität Erlangen-Nürnberg, 2024.

[35] FAST ComTec. *TA1000B-10/-50/-100/-200 Fast Pulse / Timing Preamplifier datasheet.* 2016. URL: `https://www.fastcomtec.com/fwww/datashee/amp/ta1000b.pdf` (visited on 11/24/2024).

[36] Adrian Zink. personal correspondence. 2024.

[37] Mini-Circuits. *Coaxial Reflectionless Low Pass Filter ZXLF Series.* URL: `https://www.minicircuits.com/pdfs/ZXLF-K221+.pdf` (visited on 11/24/2024).

[38] Messi & Paoloni. *Airborne 5 datasheet.* 2019. URL: `https://messi.it/dati/immagini/00017-MeP-AB5-CABLES-FULL-LIST-AIRBORNAll12-EN.pdf` (visited on 11/24/2024).

[39] Spectrum Instrumentation. *Spectrum M4i.22xx-x8 - 8 bit Digitizer datasheet.* 2024. URL: `https://spectrum-instrumentation.com/dl/m4i22_datasheet_english.pdf` (visited on 11/24/2024).

[40] Christopher W. Stubbs, F. William High, Matthew R. George, Kimberly L. DeRose, et al. "Toward More Precise Survey Photometry for PanSTARRS and LSST: Measuring Directly the Optical Transmission Spectrum of the Atmosphere". In: *Publications of the Astronomical Society of the Pacific* 119.860 (Oct. 2007).

Publisher: The University of Chicago Press, p. 1163. ISSN: 1538-3873. DOI: `10.1086/522208`. URL: `https://dx.doi.org/10.1086/522208`.

[41] Andreas Zmija. personal correspondence. 2024.

[42] Semrock. *MyLight - Semrock Online Filter Modeling Tool.* URL: `https://www.idex-hs.com/resources/tools-drawings/mylight-tutorial` (visited on 11/24/2024).

[43] A. Quirrenbach, D. Mozurkewich, D. F. Buscher, C. A. Hummel, and J. T. Armstrong. "Angular diameter and limb darkening of Arcturus." In: 312 (Aug. 1996), pp. 160–166.

[44] I. Ramírez and C. Allende Prieto. "FUNDAMENTAL PARAMETERS AND CHEMICAL COMPOSITION OF ARCTURUS". In: *The Astrophysical Journal* 743.2 (Nov. 2011). Publisher: The American Astronomical Society, p. 135. ISSN: 0004-637X. DOI: `10.1088/0004-637X/743/2/135`. URL: `https://dx.doi.org/10.1088/0004-637X/743/2/135`.

Acknowledgements

First I would like to express my gratitude to my family and everyone else who supported me during the preparation of this thesis and my studies in general. I have to extend special thanks to:

- Prof. Dr. Stefan Funk for giving me the opportunity to work on a topic in a positively fascinating and perhaps underappreciated niche field of study.
- Dr. Andreas Zmija for supervising me throughout the project, always being available to offer guidance, advice and insight immensely helpful in improving my coding, keeping a clear goal and path to it and understanding the intricacies of intensity interferometry. I am further grateful to Andreas for sharing several observation and test measurement nights with me on the roof of our institute, keeping me company and helping setting up and stowing away the telescopes.
- Naomi Vogel for supervising me throughout the project, particularly for helping my understanding of the data analysis and making better stylistic choices in presentations and this thesis.
- Dr. Adrian Zink for sharing his vast knowledge and expertise in all things hard- and software, always lending a helping hand getting any instrument or code to work, and to work better the next time it is used. He also deserves further gratitude for sacrificing many evenings and nights getting the telescopes onto the roof ready to measure and assisting in observations.
- Pedro Silva Batista for offering advice on coding and statistical analysis, being a big source of motivation through sharing his optimism. I am also thankful for keeping me company through several observation nights and helping stow away the telescopes in the early morning hours despite having to attend or even organize meetings just hours later.
- Prof. Dr. Gisela Anton for sharing her vast experience through helpful comments in our group meetings and inspiring conversations.
- Dr. Johannes Schäfer for addressing concerns — work-related or not — with positivity, empathy and a perfect dose of sarcasm, helping maneuver the different phases of my thesis project and life itself. I am also particularly grateful to him for teaching me how to get into computer-aided design and 3D-printing.
- Dr. Sebastian Ingenhütt for reviewing my thesis despite his background in a completely unrelated field and being a rad big brother.
- both the small astro-quantum optics and the larger gamma astronomy working groups for welcoming me and letting me take part in the exchange between scientists at many different stages across very different fields, providing helpful comments on presentations for conferences and creating a pleasant working environment.

Declaration of Originality

I, Christopher Ingenhütt, student registration number: 21676356, hereby confirm that I completed the submitted work independently and without the unauthorized assistance of third parties and without the use of undisclosed and, in particular, unauthorized aids. This work has not been previously submitted in its current form or in a similar form to any other examination authorities and has not been accepted as part of an examination by any other examination authority.

Where the wording has been taken from other people's work or ideas, this has been properly acknowledged and referenced. This also applies to drawings, sketches, diagrams and sources from the Internet.

In particular, I am aware that the use of artificial intelligence is forbidden unless its use an aid has been expressly permitted by the examiner. This applies in particular to chatbots (especially ChatGPT) and such programs in general that can complete the tasks of the examination or parts thereof on my behalf.

Any infringements of the above rules constitute fraud or attempted fraud and shall lead to the examination being graded "fail" ("nicht bestanden").

Place, Date	Signature